Fast Radio Bursts as a Probe for the Epoch of Reionisation

Characterising Reionisation via τ_{CMB}-DM Correlation Statistics

Author: **Dewy Peters**
Supervisor: **dr. P. Daniel Meerburg**

A thesis submitted in fulfillment of the requirements for the degree BSc in Physics

university of groningen

faculty of science and engineering

Van Swinderen Institute for Particle Physics and Gravity
Faculty of Science and Engineering
University of Groningen
The Netherlands
March 2022

1. Abstract

Despite their origin still being shrouded in mystery, Fast Radio Bursts (FRBs) allegedly have significant potential as cosmological probes. Detecting these signals at high redshifts ($z > 6$) may allow us to learn about the Intergalactic Medium (IGM) they have to traverse, and in particular the Epoch of Reionisation (EoR). This is due to the signals being dispersed along the line of sight. Another phenomenon that has quite famously been employed to study the aforementioned period of cosmic history is a map of the anisotropies in the Cosmic Microwave Background (CMB), some of which are induced by Thomson scattering during reionisation and many of which are primordial fluctuations. Therefore, a cross-correlation between the Dispersion Measure (DM) of FRBs and anisotropies in the optical depth to Thomson scattering of the CMB (τ_{CMB}) is expected to be very high and therefore may be an invaluable tool in probing the EoR. In this thesis, we indeed find that this is the case, with the correlation being consistently above 98% for multipoles between $\ell = 500$ and $\ell = 4000$. We also find the signal to be significantly in excess of the noise in all the cases we simulate. In particular, we find that the Signal to Noise Ratio (SNR) is strongly dependent on the number of FRB detections up to values of $\sim 10^9$ and that it is limited by the noise of the τ_{CMB}. Using the population synthesis program, `frbpoppy` we simulate the total SNR as a function of the maximum angular wavenumber ℓ_{max} for a series of surveys and find all to have SNRs in excess of unity, with a "perfect" survey returning values on the order of ~ 100. We therefore find that the τ_{CMB}-DM cross-correlation indeed has potential to be used as a cosmological probe in the wake of data from upcoming FRB and CMB surveys.

Contents

2. Introduction

2.1. What are Fast Radio Bursts and what can we use them for?

FRBs are bright ($\sim 1\,\text{Jy}$) and transient millisecond ($\sim 1 - 10\,\text{ms}$) radio pulses (Rafiei-Ravandi et al. 2020). Although their origin is not yet fully understood, the cosmological distances over which they are observable lends them to be a useful probe for the media they traverse (Beniamini et al. 2021; Madhavacheril et al. 2021). In the case of FRBs being detected at high redshifts ($z > 6$), this includes the IGM which was in the process of being reionised. The extent to which this took place can be determined from the DM of the signal: that is the free-electron column density along the line of sight. Since Compton scattering (the process that occurs when the photons emitted by the FRB encounter free electrons) is frequency-dependent, the signal is highly dispersed.

2.2. What is the Epoch of Reionisation?

When the universe cooled to a sufficient low temperature at $z = 1080$, free electrons combined with protons to form Hydrogen atoms: at this point, the universe became electrically neutral. After the first galaxies formed by $z \sim 11$ (eg. Oesch et al. (2016)), their integrated starlight began relieving hydrogen[1] atoms in the IGM of their lone electrons. This process continued until $z \sim 6$, at which point the IGM was overwhelmingly ionised: that is, the universe once again became predominantly populated by free protons and electrons (McGreer et al. 2014). The absence of Gunn-Peterson troughs[2] in the spectra of quasars just below $z \sim 6$ has provided the strongest corroboration of this transition (Gunn & Peterson 1965). The time-frame over which this process took place is known as the EoR. Many unanswered questions remain about this epoch. When exactly did it begin? How long exactly did it take? Was the process smooth or inhomogeneous?

2.3. How do we use FRBs to probe the Epoch of Reionisation?

In this thesis, we investigate how cross-correlating the DMs of FRBs with fluctuations in the optical depth of the Cosmic Microwave Background (CMB), τ_{CMB} can be used to improve our knowledge of the EoR[3]. To this end, we test the efficacy of such a correlation on an existing reionisation model, that of Namikawa et al. (2021). Thus, in Sec. 3, we describe its most important features and how τ_{CMB} the DM relate to it. Then, in Sec. 4, we derive the cross-correlation function $C_\ell^{\tau\text{DM}}$ and the coefficient $|\alpha|_\ell^{\tau\text{DM}}$ to measure the extent of correlation. In Sec. 5, we derive the Signal-to-Noise Ratio (SNR) of the $\tau_{\text{CMB}} - \text{DM}$ cross-correlation, examine its dependence on the number of FRB detections and use a population synthesis program, `frbpoppy` to simulate a series of surveys (Gardenier et al. 2019). We then conclude with a discussion of the results in Sec. 6 The objective of this thesis is therefore to assess the extent of the τ_{CMB}-DM correlation and the forecast its SNR.

2.4. What fundamental questions could this cross-correlation help answer in the future?

Being able to characterise the Universe's reionisation history by mapping the free electron number density via τ_{CMB} and FRB DMs is an important prerequisite for studying the Universe at $z > 6$. This includes not only better constraints on the duration and homogeneity of reionisation but also the cosmological growth rate (Madhavacheril et al. 2021), the size and distribution of ionised bubbles forming around baryonic matter (Namikawa et al. 2021), the ionisation efficiency of integrated starlight from the first galaxies (Wyithe & Loeb 2003), and constraints on the star formation efficiency of galaxies sourcing the EoR (Sun & Furlanetto 2016).

---

[1]Helium atoms were also ionised but slightly later than hydrogen ones, owing to their greater ionisation energies. Additionally, there were two stages of He-reionisation: that of neutral helium, HeI and that of HeII, singly ionised. The latter took place between $z \sim 3$ and 4. (Sokasian et al. 2002)

[2]Which constitute the suppression wavelengths shorter than that of the Lyman-α. This occurs due to the bound electron in neutral hydrogen absorbing it along the line-of-sight. The absence of these troughs at lower redshifts therefore implies that most of the hydrogen has been ionised.

[3]Wherever τ is mentioned within this thesis, it refers to τ_{CMB}. We use these interchangeably in order to avoid convoluted notation where possible.

3. Physical Model

This section details the entire physical model used in performing the cross-correlation between the τ_{CMB} anisotropies and the DMs of FRBs. Since we are primarily interested in these quantities to constrain teh reionisation history during the EoR, we begin this section with an assumed reionisation model, embodied by the ionisation fraction, x_e, and the three-dimensional power spectrum of density-weighted ionisation fraction fluctuations, $P_{x_e x_e}$ (Namikawa et al. 2021). We then describe how the two observables, τ_{CMB} and DM depend on it. This will then motivate the cross-correlation which will be performed in the following section.

3.1. Reionisation Model

In order to determine the correlation function of the τ_{CMB} and DM fields, we first need to compute $P_{x_e x_e}$. It is this quantity that embodies the reionisation model and is traced by both τ_{CMB} and DM. Since deriving it is beyond the scope of this thesis, we summarise it by presenting the z-dependence of the average ionisation fraction, $\bar{x}_e$ and the bubble-size distribution, $P(r)$ along with parameter values used by Namikawa et al. (2021). We plot $P_{x_e x_e}$ in Sec. 3.1.3 for three different redshifts corresponding to points along the EoR, at $z = 5, 7.5$ and 11 Since we obtained the code to generate $P_{x_e x_e}$ from Namikawa et al. (2021), we use the same values by default. For a full derivation of $P_{x_e x_e}$ from x_e and $P(r)$, see Dvorkin & Smith (2009).

3.1.1. Ionisation Fraction

The ionisation fraction, x_e is defined as the ratio of the number density of free electrons, n_e to the total number density, n in a given medium. Its mean value across the universe, $\bar{x}_e$ is by definition, the principal quantity of the EoR. We parameterise it in the following way, in order to maintain consistency with Dvorkin & Smith (2009) and Lewis et al. (2000):

$$\bar{x}_e(z) = \frac{1}{2}\left[1 - \tanh\left(\frac{y(z) - y_{\mathrm{re}}}{\Delta_y}\right)\right] \tag{1}$$

where $y(z) = (1+z)^{3/2}$, $y_{\mathrm{re}} = y(z_{\mathrm{re}})$ and Δ_y are free parameters of the model. In this case, we assume $z_{\mathrm{re}} = 7.5$. That is, the redshift at which $\bar{x}_e = 0.5$. Furthermore, we take $\Delta_y = 19.0$ as in Dvorkin & Smith (2009). In Fig. 1, we show the corresponding plot of the average ionisation fraction as a function of redshift.
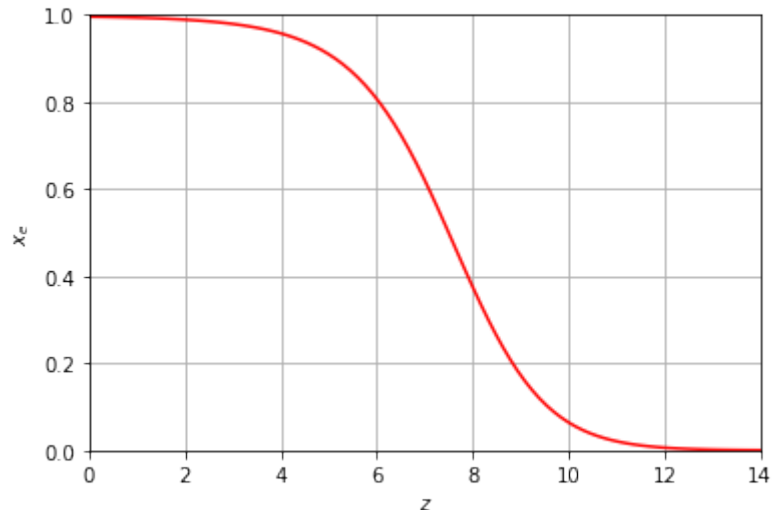

Fig. 1. The average ionisation fraction as a function of redshift.

Fig. 1 is consistent with Gunn & Peterson (1965); McGreer et al. (2014) and Kulkarni et al. (2019) in its implication that reionisation was complete by $z \sim 5$.

3.1.2. Bubble-size Distribution

It is conceptually beneficial to think of large-scale cosmic structure since the onset of reionisation as being comprised of HII regions or "bubbles" of ionised material enveloping galaxy clusters, with filaments of neutral matter lying beyond. Here, we assume that the bubble sizes follow a log-normal distribution given by:

$$P(r) = \frac{1}{r} \frac{1}{\sqrt{2\pi\sigma_{\ln r}^2}} \exp\left\{ -\frac{[\ln(r/R_b)]^2}{2\sigma_{\ln r}^2} \right\} \tag{2}$$

where R_b is the characteristic radius of the ionised bubbles, $\sigma_{\ln r}$ is the width of the distribution, and r is the radial spatial coordinate (Dvorkin & Smith 2009). This distribution is predicated on the assumption that the number density of bubbles fluctuates as a biased tracer of large scale structure. The bias arises from the fact that at higher redshifts when these bubbles are in their early stages of formation, they tend to appear in the densest regions (Furlanetto et al. 2004). In this thesis, we set $R_b = 5\,\text{Mpc}$ and $\sigma_{\ln r} = \ln 2$. This is because we use the code of Namikawa et al. (2021) and these are the default values therein.
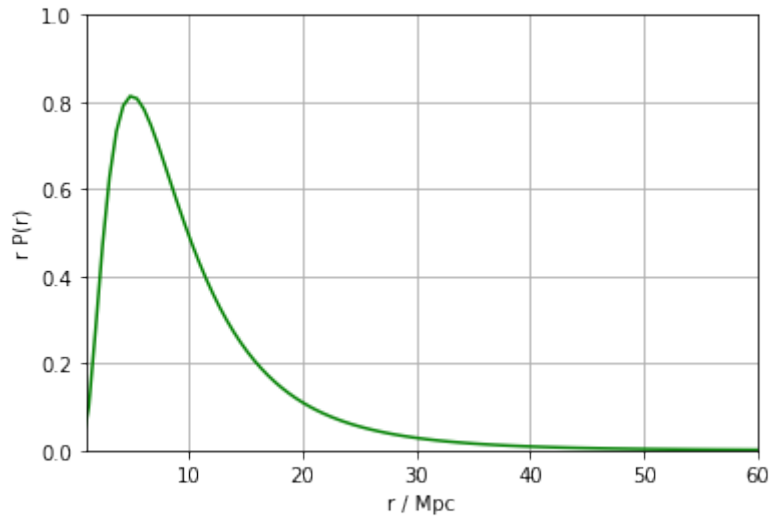
Fig. 2. The Bubble-size Distribution as a function of radius.

3.1.3. Free Electron Power Spectrum

Here we present the profile of $P_{x_e x_e}$ with respect to wavenumber, k. We have chosen to plot it for three different redshifts: the first, $z = 5$ corresponding to the end of the EoR; the second, $z = 7.5$, roughly corresponding to the halfway points of the EoR and $z = 11$, corresponding to an earlier point in the EoR. This graph is displayed is to clarify the reionisation model we use.
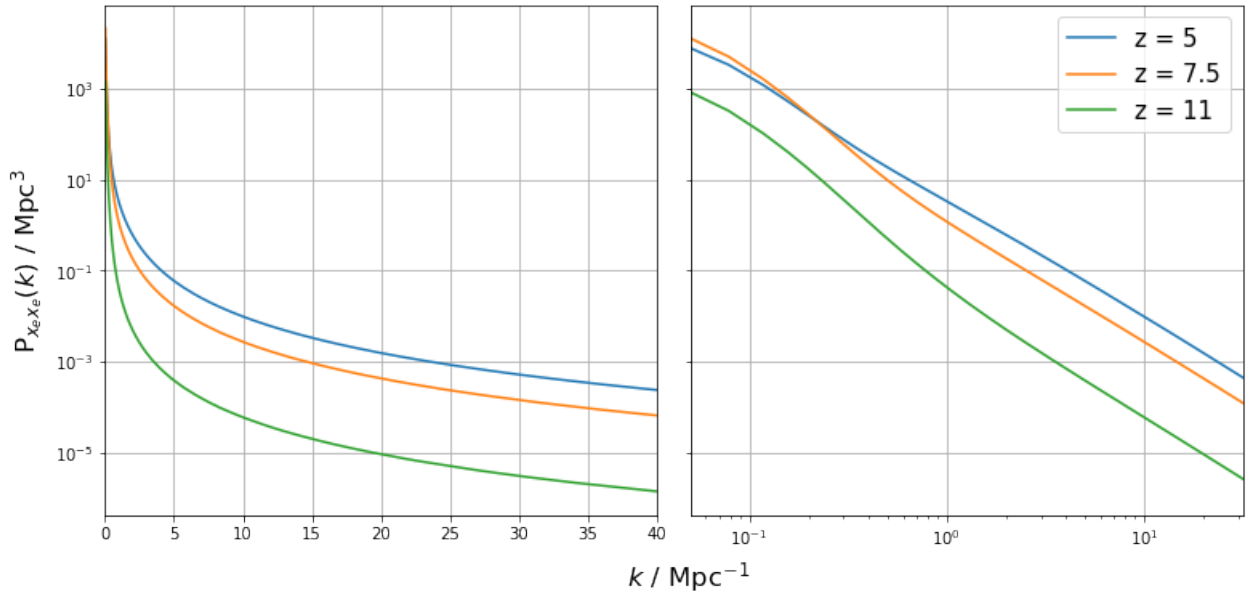
Fig. 3. The Power Spectrum, $P_{x_e x_e}$ plotted at redshifts of 5, 7.5 and 11. In the scale of the x-axis on the right tile is logarithmic.

As would be expected, $P_{x_e x_e}$ values would be larger at lower redshifts given that more of the EoR has elapsed and therefore there are more free electrons to contribute to the ionisation fraction x_e.

3.2. CMB Optical Depth Anisotropies

As indicated previously, fluctuations in τ_{CMB} trace the underlying free electron number density. This is because radiation emitted at the surface of last scattering would have had to traverse the IGM during the EoR in order for us to observe it. When the CMB photons encountered free electrons during the EoR, they would have experienced Thomson scattering: a process unique to ionised matter. We therefore begin this section by defining the reionisation optical depth and explaining the process of Thomson scattering. We then examine the redshift dependence of τ_{CMB} in order to infer its utilities and caveats in constraining reionisation.

3.2.1. Reionisation Optical Depth

Optical depth, τ is a measure of the radiant power transmitted through a medium given its incidence. In this case, it is the fraction of the CMB transmitted through the IGM during the EoR and therefore connected to the integrated electron density along the line of sight. There are several physical processes the facilitate this interaction: Thomson scattering, whereby photons are non-relativistically and elastically scattered by free electrons; the screening mechanism, whereby initially E-mode[4] photons are re-polarised by free electrons as B-mode[5] ones (Dvorkin et al. 2009); and the kinematic Sunyaev-Zeldovich (kSZ) effect, whereby photons inelastically Compton scatter of free electrons that have non-zero peculiar velocities with respect to the photons' original rest frame (Sunyaev & Zeldovich 1980). We only detail Thomson scattering here as a detailed treatment of the latter two processes is beyond the scope of this thesis. We refer the reader to Dvorkin et al. (2009) and Dvorkin & Smith (2009) for a more detailed treatment of these phenomena.

3.2.2. Thomson Scattering

Thomson scattering was the fundamental process responsible for secondary contributions to observed CMB anisotropies during the EoR. In this case, it occurred when the electric field of the incident CMB radiation accelerated free electrons during the EoR which in turn re-radiated it at the same frequency. As the low-energy limit of Compton scattering (Chen et al. 1998), it necessitates the interaction to be non-relativistic and therefore implies the photon energy being much smaller than the mass energy of the electron, $E_\gamma = h\nu_\gamma \ll m_e c^2$. By the EoR, the vast majority of CMB photons were

---

[4]The electromagnetic plane wave has an up-down bearing
[5]The electromagnetic plane wave is crossed at 45°

comfortably within this regime. Over the course of that epoch, n_e increased as more and more hydrogen atoms were relieved of their concomitant electrons captured during recombination.

The optical depth due to Thomson scattering over a comoving distance, χ and along the line of sight, $\hat{n}$ is given by

$$\tau(\chi, \hat{n}) = \sigma_T \int_0^{\chi} n_e(\chi', \hat{n}) a(\chi') d\chi' \tag{3}$$

where σ_T is the Thomson scattering cross-section, $a(\chi')$ is the scale factor of the Universe and $n_e(\chi', \hat{n})$ is the free electron number density (Meerburg et al. 2013). If we wish to constrain the ionisation fraction, x_e we can use the relation

$$n_e(\chi, \hat{n}) \simeq \left(1 - \frac{3}{4} Y_p\right) \frac{\rho_b}{m_p} x_e(\chi, \hat{n}) \tag{4}$$

where ρ_b is the baryonic mass density, m_p is the proton mass and the factor $\left(1 - \frac{3}{4} Y_p\right)$ accounts for Helium being singly ionised (Meerburg et al. 2013).

We can formalise the CMB anisotropies by dimensionlessly quantifying departures from the average baryonic density field, $\bar{\rho}_b$ with the parameter

$$\delta_b = \frac{\rho_b - \bar{\rho}_b}{\bar{\rho}_b} \tag{5}$$

which we refer to in this text as the baryonic overdensity. Rearranging this and using the substitution $\bar{\rho}_b = \rho_{b0}/a^3$ for the average baryonic mass density, we find that

$$\rho_b = \frac{\rho_{b0}}{a^3}(1 + \delta_b) \tag{6}$$

so

$$n_e = \left(1 - \frac{3}{4} Y_p\right)(1 + \delta_b) \frac{x_e \rho_{b0}}{m_p a^3} \tag{7}$$

and the optical depth becomes

$$\tau(\chi, \hat{n}) = \sigma_T \left(1 - \frac{3}{4} Y_p\right) \frac{\rho_{b0}}{m_p} \int_0^{\chi} \frac{x_e(\chi', \hat{n})}{a^2(\chi')}(1 + \delta_b(\chi', \hat{n})) d\chi' \tag{8}$$

where ρ_{b0} is the baryonic mass density at present and $\hat{n}$ is the unit normal vector (Meerburg et al. 2013).

3.2.3. Redshift Dependence

Now that we have explained the Thomson scattering contribution to τ_{CMB}, we present its z-dependence in the reionisation model we use. As we shall see in Sec. 3.3, it differs from the DM in that it is an indirect probe of the integrated electron column density, with additional $a(\chi')$ and σ_T contributions. The profile obtained is given in Fig. 4 below.
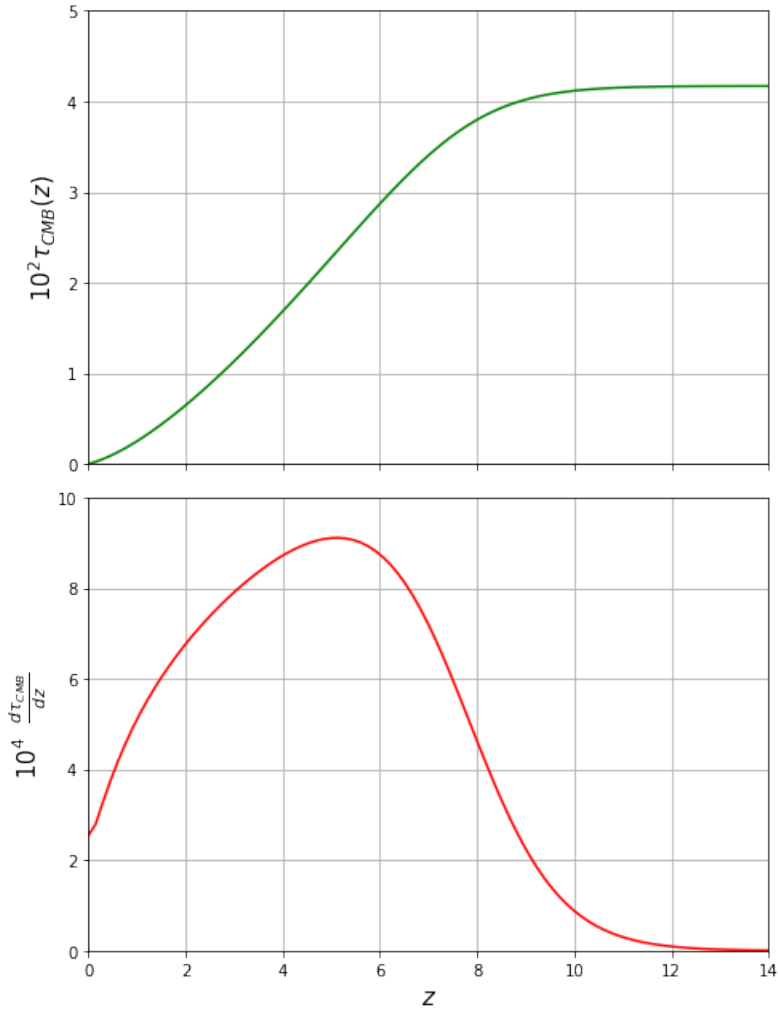
Fig. 4. Upper panel: the redshift profile of the optical depth to Thomson scattering multiplied by a factor of 100. Lower panel: the redshift gradient of the optical depth to Thomson scattering multiplied by a factor of 10 000.

In Fig. 4 it can be seen that Thomson scattering optical depth experiences a steep increase with redshift and saturates at $z \sim 10$, the begining of the EoR. It can also be seen that the gradient of τ_{CMB} reaches its maximum at $z \sim 5$, just after the EoR. Both of these behaviours are to be expected from the reionisation model: the former as the universe was effectively neutral at $z \sim 10$ so there were significantly fewer free electrons to Thomson scatter the CMB and only the free electrons at lower redshifts contribute; the latter as reionisation was effectively complete by $z \sim 5$ so there were fewer fresh free electrons to contribute to τ_{CMB}.

3.3. Dispersion Measure of FRBs

We propose using FRBs to probe the EoR, like τ_{CMB}, via their interaction of their signals with free electrons along the line of sight. In this subsection, we begin by describing the process of dispersion in order to formulate the DM. We then explain all the contributions to this quantity and clarify those which need to be subtracted. Finally, as for the CMB Optical Depth anisotropies, we present the z-dependence of the DM resulting from the reionisation model we have adopted.

3.3.1. FRB Dispersion

Like all radiation, the burst is emitted across a range of frequencies which interact differently depending on the nature of the matter they encounter. The net result of this is a frequency-dependent arrival time for the signal: components of higher frequencies arrive before those at lower ones. This difference is principally down to the scattering by free electrons

in the IGM. In the case of FRBs, the arrival time of a signal at frequency ν_0 in the observer frame relative to the moment of arrival of a signal travelling at c from the same source is given by

$$t = \frac{q^2}{2\pi m_e c \nu_0^2} \int_0^\chi n_e(\chi', \hat{n}) a^2(\chi') d\chi' \tag{9}$$

where

$$\chi = c \int_0^z \frac{dz'}{H(z')} = \frac{c}{H_0 \Omega_{m0}^{1/2}} \int_0^z \frac{dz'}{[(1+z')^3 + \Omega_{\Lambda,0}/\Omega_{m0}]^{1/2}} \tag{10}$$

is the comoving distance to an FRB at redshift, z; $d\chi'$ is the comoving length of the segment; $n_e(\chi', \hat{n})$ is the proper density of electrons; $a(\chi')$ is the scale factor of the universe, c is the speed of light, q is the electron charge and m_e is the electron mass (Beniamini et al. 2021).

3.3.2. Dispersion Measure

This differential arrival time motivates a quantity known as the DM. Since this is down to the scattering by free electrons, the DM is defined as the integral of the electron column density along the line of sight:

$$\text{DM} = \int_0^\chi n_e(\chi', \hat{n}) d\chi' \tag{11}$$

As previously stated in Sec. 3.2.3, this differs from τ_{CMB} in that it directly measures the free electron column density. It is also frequently used in the context of pulsars to probe HII regions in the Milky Way.

3.3.3. Contributions to the DM

It should be noted that free electrons in the IGM are not the sole contributors to the DM. More generally, the total DM of an FRB is the sum of three components:

$$\text{DM} = \text{DM}_{\text{MW}} + \text{DM}_{\text{H}} + \text{DM}_{\text{IGM}} \tag{12}$$

where DM_{MW} is the local contribution from the Milky Way, DM_{H} is the contribution from the FRB's host galaxy and DM_{IGM} is the IGM contribution that we are most interested in (Rafiei-Ravandi et al. 2020). For precision measurements, DM_{MW} can be easily determined and subtracted whilst DM_{H} would require the FRB to be localised. However, given the vast cosmological distances of the IGM, the DM_{IGM} contribution should significantly exceed that of the two former terms. Therefore, for the purposes of this thesis, we shall assume that $\text{DM} \sim \text{DM}_{\text{IGM}}$ and ignore the other two contributions.

The galactic distribution of free electrons has been relatively well constrained by measurements of pulsar DMs (Taylor & Cordes 1993; Ioka 2004). As would be expected given the distribution of matter in the Milky Way, the maximum DM, $\text{DM}_{\text{MW}}^{\text{max}} \sim 10^3 \, \text{pc} \, \text{cm}^{-3}$ occurs parallel to the galactic plane, and the minimum DM, $\text{DM}_{\text{MW}}^{\text{min}} \sim 30 \, \text{pc} \, \text{cm}^{-3}$ occurs perpendicular to the galactic plane (Nordgren et al. 1992; Taylor & Cordes 1993; Ioka 2004). Whilst the contribution of the Milky Way may interfere with constraining DM_{IGM} at low redshifts for objects such as FRB181030 (CHIME/FRB Collaboration et al. 2019), for us it will pose little risk. At the time of writing, the largest measured value of the DM of an FRB is $2500 \, \text{pc} \, \text{cm}^{-3}$, corresponding to a redshift $z \sim 3$ (Zhang 2018; Beniamini et al. 2021). Given that the redshift interval we concern ourselves here with $5 \leqslant z \leqslant 10$ would correspond to even greater DM-values[6], local Milky Way contributions to the DM are unlikely to be a major source of contamination. It can safely be reasoned that DM contributions from the Milky Way would be at least an order of magnitude smaller than those of emissions from the EoR.

The main obstacle in subtracting the host contribution to the DM is localising the FRB to a galaxy to begin with. Namely, the majority of instruments to date capable of finding large numbers of FRBs have insufficient angular resolution ($> 1'$) to localise them to galaxies (Eftekhari & Berger 2017; Amiri et al. 2018; CHIME/FRB Collaboration et al. 2019; Masui et al. 2019; Rafiei-Ravandi et al. 2020). Not only this; since, FRBs do not exhibit spectral lines, their redshifts are not easy to determine without host galaxy associations. Otherwise, we have to use the inequality stipulating that the DM of the host has to be greater than or equal to nil, $\text{DM}_{\text{H}} \geqslant 0$ which in turn implies an upper bound on the redshift due to the relation. This, however, is not immune to the hypothesis that FRBs, even at low redshifts, have intrinsically large host DMs - a seemingly dubious line of reasoning.

---

[6] Owing to the larger IGM distances traversed

3.3.4. Redshift Dependence

Before describing the DM redshift profile model put to use in this thesis, it should be noted that DM_{IGM} increasingly dominates Eqn. (12) at higher redshifts. Conversely, this implies that lower redshift observations are subject to more contamination by free electron overdensities locally in the Milky Way and in the host galaxy of the FRB, as the vast majority of FRBs recorded to date are extragalactic to begin with.
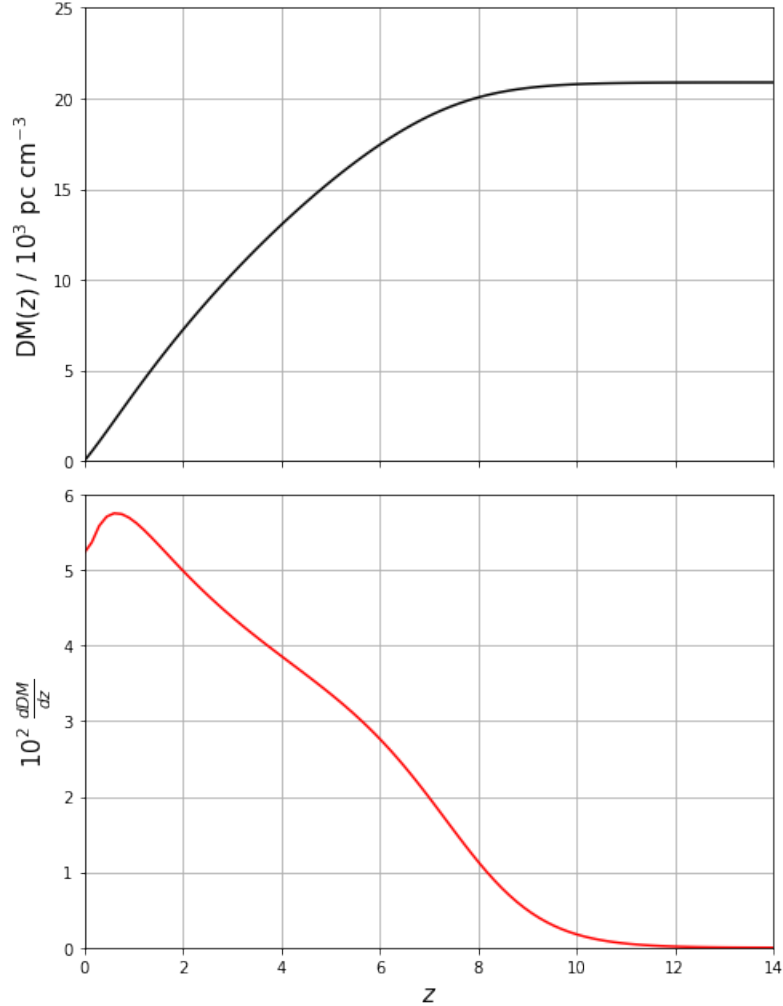
Fig. 5. Top panel: the DM as a function of redshift in units of thousands of $\mathrm{pc\,cm^{-3}}$. Bottom panel: the scaled up ($\times 100$) gradient of the DM with respect to redshift.

In Fig. 5, we see that the DM initially increases rapidly with redshift until $z \sim 1$, from which point it increases with at a decreasing rate until $z \sim 10$ whereupon it begins to saturate. Physically, this signifies that at lower redshifts ($z < 5$), there are larger densities of free electrons as the EoR has for the most part already elapsed. The saturation beyond $z \sim 10$ is present as the Universe was mostly electrically neutral at the time any signal at this distance was emitted. Like Fig. 4 in the previous section, this is based on the reionisation model used by Namikawa et al. (2021). The z and DM of saturation may be increased or decreased with respect to Fig. 5 depending on the extent of correlation between the ionisation fraction and density field as shown by Pagano & Fronenberg (2021).

4. Cross-Correlation

In order for FRBs to successfully serve as a probe for the EoR, we need to establish a framework for cross-correlating the DM with the CMB Optical Depth anisotropies. Seen as both quantities are tracers of the underlying free electron density field, we need not concern ourselves with the construction of a power spectrum of two distinct variables such as that of free electrons and galaxies (ie. P_{ge}) in Madhavacheril et al. (2021); rather, $P_{x_e x_e}$ as defined in the previous section suffices for all of our correlation functions. In this section, we will begin by deriving the cross-correlation function, $C_\ell^{\tau \mathrm{DM}}$: the centrepiece of this thesis. We then introduce the two auto-correlation functions of DM and τ_{CMB} given by Madhavacheril et al. (2021) and Namikawa et al. (2021) respectively. Since they are derived in a very similar way to $C_\ell^{\tau \mathrm{DM}}$, we do not perform a full derivation. However, we do explain the origin of their associated noise terms. We conclude this section by computing the cross-correlation coefficient, α_ℓ to examine the extent to which τ_{CMB} and DM are correlated. This will then pave the way for the following section where we derive the SNR.

4.1. Cross-Correlation Function

The cross-correlation function, $C_\ell^{\tau \mathrm{DM}}$ lies at the heart of this thesis. It simulates the extent to which information on the CMB anisotropies in terms of τ_{CMB} can be dovetailed with DM measurements from FRBs. We perform a derivation of this quantity using a multipole expansion. In this case, ℓ is the angular wavenumber or number of multipoles, and x is a coordinate of position space. We assume the Limber approximation to hold throughout: that is, that Bessel functions associated with any of the terms treated are small, $j_\ell(x) \ll 1$ for $x < \ell$ and peak when $x \sim \ell$ (Meerburg et al. 2013). This results in the relation $k = \frac{\ell}{\chi}$ in Madhavacheril et al. (2021) or $k = \frac{L+1/2}{\chi}$ in Namikawa et al. (2021) where k denotes comoving wavenumber. The auto-correlation coefficients introduced in the two upcoming subsections are from Namikawa et al. (2021) and Madhavacheril et al. (2021) respectively but can be derived in a very similar way to $C_\ell^{\tau \mathrm{DM}}$.

To begin this derivation, we introduce the quantities $\tau_{\ell m}$ and $\mathrm{DM}_{\ell m}$ where m is an integer. For the optical depth, we have

$$\tau_{\ell m}(\chi) = 4\pi(-i)^\ell \int \frac{d^3 k}{(2\pi)^3} X(\boldsymbol{k}) \alpha_\ell^\tau(k) Y_{\ell m}^*(\hat{k}) \tag{13}$$

where

$$\alpha_\ell^\tau = \frac{\sigma_T \rho_{b,0}}{m_p}\left(1 - \frac{3}{4}Y_p\right) \int_0^{\chi_*} \frac{d\chi'}{a^2} j_\ell(k\chi') \tag{14}$$

and

$$X(\boldsymbol{k}) = x_e \delta_X(\bar{k}) \tag{15}$$

with x_e corresponding to the ionisation fraction, $\delta_X(\boldsymbol{k})$ corresponding to the average field overdensity and χ_* corresponding to the distance from the surface of last scattering as in Meerburg et al. (2013). We expand the Dispersion Measure in a similar manner:

$$\mathrm{DM}_{\ell m}(\chi) = 4\pi(-i)^\ell \int \frac{d^3 k}{(2\pi)^3} \bar{x}_e \delta_X(\bar{k}) \alpha_\ell^{\mathrm{DM}} Y_{\ell m}^*(\hat{k}) \tag{16}$$

where

$$\alpha_\ell^{\mathrm{DM}}(k) = n_{e0}\left(1 - \frac{3}{4}Y_p\right) \int_0^{\chi_*} \frac{d\chi'}{a} j_\ell(k\chi') \tag{17}$$

and all symbols therein have their usual meaning. Now that we have both variables framed in terms of spherical harmonics, we can perform the cross-correlation.

Firstly, we note that by definition, the cross-correlation of the two maps has the form

$$\langle \tau_{\ell m} \mathrm{DM}_{\ell' m'}^* \rangle = \delta_{\ell \ell'} \delta_{mm'} C_\ell^{\tau \mathrm{DM}}(\chi) \tag{18}$$

Substituting Eqns. (35) and (17) into Eqn. (18), we obtain

$$\langle \tau_{\ell m} \mathrm{DM}_{\ell' m'}^* \rangle = (4\pi)^2 (-i)^\ell (i)^{\ell'} \left(1 - \frac{3}{4}Y_p\right)^2 n_{e0}^2 \sigma_T \int \frac{d^3 k}{(2\pi)^3} \tilde{\alpha}_\ell^\tau(k) Y_{\ell m}^*(\hat{k}) \int \frac{d^3 k}{(2\pi)^3} \tilde{\alpha}_{\ell'}^{\mathrm{DM}}(k') Y_{\ell' m'}(\hat{k}) \langle \delta_X(\bar{k}) \delta_X^*(k') \rangle \tag{19}$$

where

$$\langle \delta_X(k) \delta_X^*(k) \rangle = (2\pi)^3 \delta(\bar{k} - \bar{k}') P_{x_e x_e}(k) \tag{20}$$

and

$$\tilde{\alpha}_\ell^\tau(k) = \int_0^{\chi*} \frac{d\chi'}{a^2} j_\ell(k\chi') \tag{21}$$

$$\tilde{\alpha}_\ell^{\mathrm{DM}}(k) = \int_0^{\chi*} \frac{d\chi'}{a} j_\ell(k\chi') \tag{22}$$

To evaluate the above integrals, we note that

$$\delta_{\ell\ell'}\delta_{mm'} = \int \frac{d^3k}{(2\pi)^3} Y_{\ell m}^*(\hat{k}) \int \frac{d^3k}{(2\pi)^3} Y_{\ell'm'}(\hat{k}) \tag{23}$$

and that

$$\int \frac{d^3k}{(2\pi)^3} = \frac{1}{(2\pi)^3} \int d\Omega \int k^2 dk \tag{24}$$

$$= \frac{1}{2\pi^2} \int k^2 dk \tag{25}$$

Therefore,

$$\delta_{\ell'\ell}\delta_{m'm} = \frac{1}{2\pi^2} \int Y_{\ell m}^*(\hat{k})k^2 dk \int Y_{\ell'm'}(\hat{k})k^2 dk \tag{26}$$

and since

$$\langle \tau_{\ell m}\mathrm{DM}_{\ell'm'}^* \rangle = (2\pi^2)C_\ell^{\tau\mathrm{DM}} \tag{27}$$

we have that

$$\langle \tau_{\ell m}\mathrm{DM}_{\ell'm'}^* \rangle = (4\pi)^2(-i)^\ell i^{\ell'} \left(1 - \frac{3}{4}Y_p\right)^2 \sigma_T \int \frac{dk}{2\pi} k^2 \tilde{\alpha}_\ell^\tau(k)\tilde{\alpha}_\ell^{\mathrm{DM}}(k)P_{x_e x_e}(k,\chi) \tag{28}$$

$$= (4\pi)^2(-i)^\ell i^{\ell'} \left(1 - \frac{3}{4}Y_p\right)^2 \sigma_T \int \frac{dk}{2\pi} k^2 P_{x_e x_e}(k,\chi) \int_0^{\chi*} \frac{d\chi}{a} j_\ell(k\chi) \int_0^{\chi*} \frac{d\chi'}{a^2} j_\ell(k\chi') \tag{29}$$

Under the Limber approximation, we can assume that $j_\ell(k\chi) \ll 1$ for $x < \ell$ and peak when $x \sim \ell$. The integral over k receives the greatest contribution from the modes $k \sim \ell/\chi$. This also allows us to perform the k-integral over the product of Bessel functions as:

$$\int_0^\infty dk k^2 j_\ell(k\chi)j_\ell(\chi') = \frac{\pi}{2}\frac{\delta(\chi - \chi')}{\chi^2} \tag{30}$$

Therefore, we have that

$$\langle \tau_{\ell m}\mathrm{DM}_{\ell'm'}^* \rangle = \frac{1}{2\pi}\frac{\pi}{2}(4\pi)^2(-i)^\ell i^{\ell'} \left(1 - \frac{3}{4}Y_p\right)^2 \sigma_T \int \frac{d\chi}{a}\frac{d\chi'}{a^2}\frac{\delta(\chi - \chi')}{\chi^2}P_{x_e x_e}(\ell/\chi,\chi') \tag{31}$$

and

$$C_\ell^{\tau\mathrm{DM}} = \frac{1}{2\pi}\frac{\pi(4\pi)^2}{2(2\pi^2)}(-i)^\ell i^{\ell'} \left(1 - \frac{3}{4}Y_p\right)^2 \sigma_T \int \frac{d\chi}{a}\frac{d\chi'}{a^2}\frac{\delta(\chi - \chi')}{\chi^2}P_{x_e x_e}(\ell/\chi,\chi') \tag{32}$$

which evaluates to

$$C_\ell^{\tau\mathrm{DM}} = \sigma_T n_{p,0}^2 \left(1 - \frac{3}{4}Y_p\right)^2 \int \frac{d\chi}{\chi^2 a^3}P_{x_e x_e}(\ell/\chi,\chi) \tag{33}$$

Now that we have derived $C_\ell^{\tau\mathrm{DM}}$, we present its ℓ-profile as a multiple of $\ell(\ell+1)$ for the graph to look more presentable. The scale begins at $\ell = 500$ as the Limber approximation begins to break down with lower numbers of multipoles. The logarithmic profile is shown in Fig. 6.
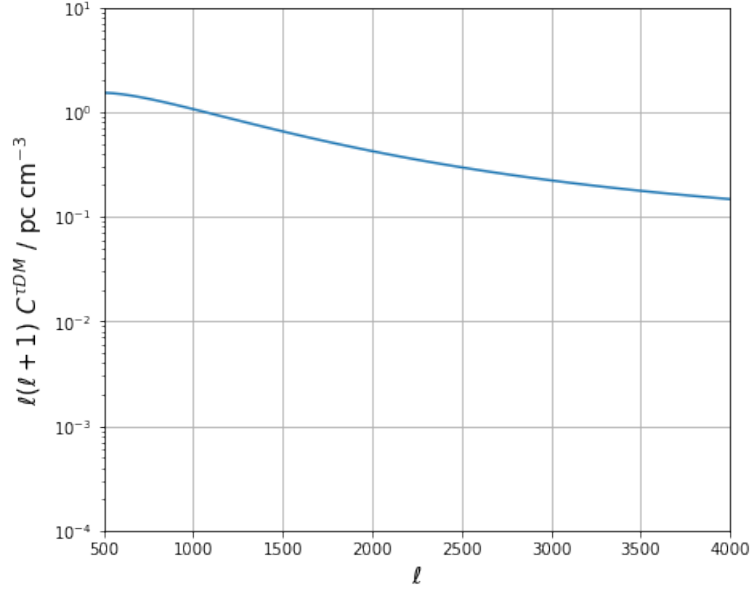
Fig. 6. The angular cross-correlation power spectrum of the Optical Depth to Thomson scattering and Dispersion Measure.

In Fig. 6, we see that the product of the cross-spectrum and the factor $\ell(\ell+1)$ declines steadily with the number of multipoles on a logarithmic scale.

4.2. Auto-Correlation Functions

In this subsection, we introduce the auto-correlation functions, C_ℓ^{DMDM} and $C_\ell^{\tau\tau}$ as defined in Madhavacheril et al. (2021) and Namikawa et al. (2021) along with their associated noise terms. As previously, the Limber approximation is assumed. Their derivation is performed in a very similar way to that of $C_\ell^{\tau\mathrm{DM}}$; the only difference being that $\tau_{\ell m}$ is replaced by $\mathrm{DM}_{\ell m}$ in the case of the DM auto-correlation and that $\mathrm{DM}_{\ell m}$ is replaced with $\tau_{\ell m}$ in the case of the τ_{CMB} auto-correlation.

4.2.1. Dispersion Measure

From Madhavacheril et al. (2021) we have that the angular auto power spectrum of FRB DMs is given by

$$C_\ell^{\mathrm{DMDM}} = n_{e0}^2 \int \frac{P_{x_e x_e}(k = \ell/\chi, \chi)}{a^2 \chi^2} d\chi' \tag{34}$$

where n_{e0} is the free electron number density at present, a is the scale factor of the Universe and $P_{x_e x_e}(k = \ell/\chi, \chi)$ is the free electron auto power spectrum evaluated under the Limber approximation. Eqn. (34) is derived in exactly the same way as $C_\ell^{\tau\mathrm{DM}}$: the only difference is that $\tau_{\ell m} \to \mathrm{DM}_{\ell m}$. The corresponding profile is plotted logarithmically in Fig. 9.
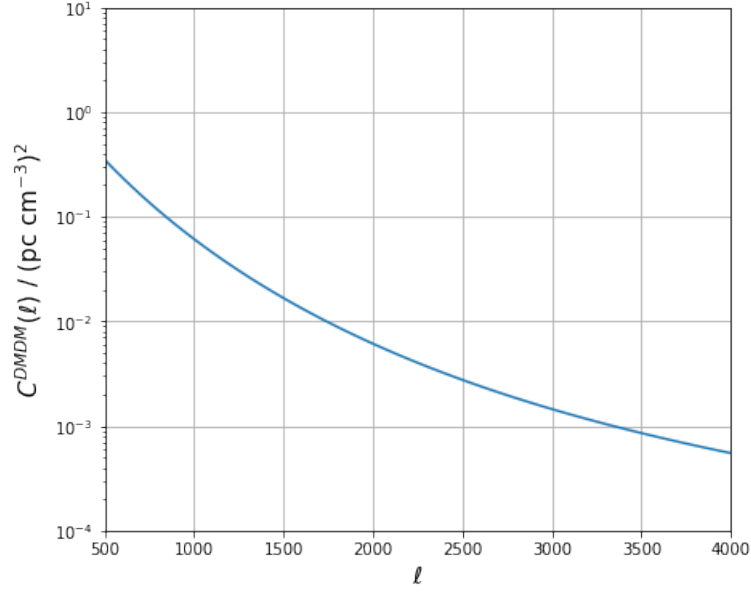
Fig. 7. The angular auto-correlation power spectrum of the Dispersion Measure.

It can be seen from Fig. 9 that the the auto-correlation decreases exponentially with the number of multipoles.

4.2.2. CMB Optical Depth

From Namikawa et al. (2021) we have that the angular auto power spectrum is given by

$$C_\ell^{\tau\tau} = \sigma_T^2 n_{e0}^2 \int \frac{d\chi}{a^4 \chi^2} P_{x_e x_e}(k = \ell/\chi, \chi) \tag{35}$$

where σ_T is the Thomson scattering cross-section and n_{e0} is the free electron number density at present. In this thesis we assume this quantity to be similar to the corresponding term for protons, $n_{p0} \sim n_{e0}$. Notice the $P_{x_e x_e}(k = \ell/\chi, \chi)$ term which is also present for the DM.

Fig. 8. The angular auto-correlation power spectrum of the CMB Optical Depth Anisotropies with the noise spectrum superimposed. Note the factor $\ell(\ell+1)/2\pi$ multiplying the auto-correlation power spectrum. This factor is absent in the noise spectrum.

4.3. Cross-correlation Coefficient

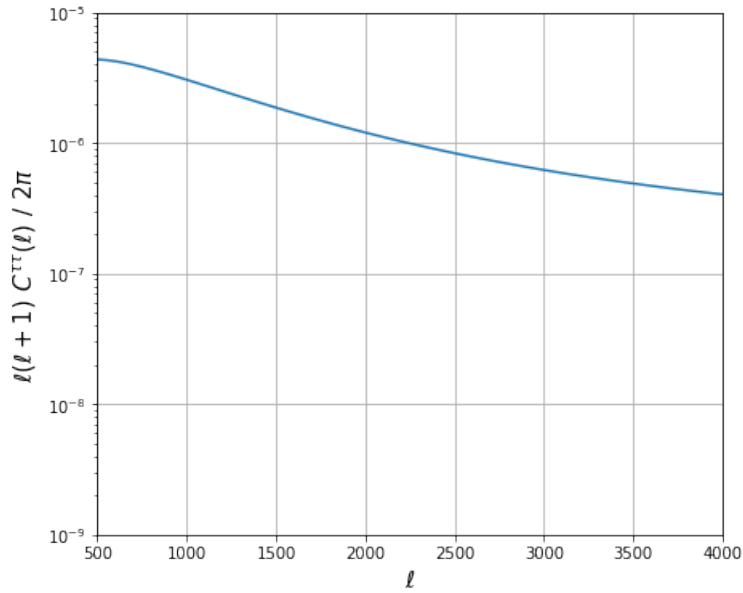Given the mutual dependence on the power spectrum, $P_{x_e x_e}$, DM and τ_{CMB} are expected to be highly correlated. Where the variables differ is in the scale factor dependence and the constant prefactors. Whilst DM contributes n_{e0} and varies as $1/a$, τ_{CMB} contributes σ_T in addition to $n_{e,0}$ and is proportional to $1/a^2$. We can define the cross-correlation coefficient as

$$|\alpha_\ell|^2 = \frac{\left(C_\ell^{\tau \mathrm{DM}}\right)^2}{C_\ell^{\tau\tau} C_\ell^{\mathrm{DMDM}}} \tag{36}$$

This cross-correlation coefficient serves as a convolution of each of the integrals defining the correlation functions. As a result, any deviation from unity would likely be the result of different scale factor dependencies.
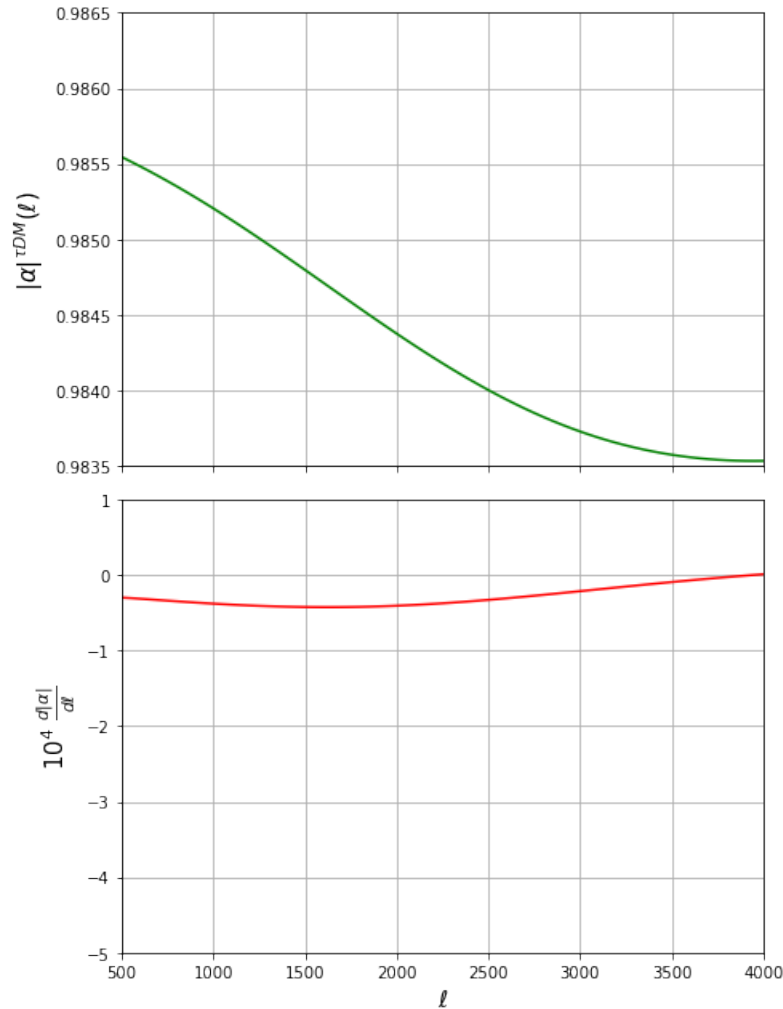
Fig. 9. Top panel: the cross-correlation coefficient as a function of angular wavenumber or multipoles, ℓ. Bottom panel: the profile of the slope in $|\alpha|$ with respect to ℓ. Note that the latter has been scaled up by a factor of 10^4.

In Fig. 9 we see that the correlation coefficient does indeed deviate from unity. There are several important things to note here. Firstly, the scale of the plot: the entire curve lies in the $|\alpha|^{\tau \mathrm{DM}}$ interval $[0.9835, 0.9865]$ and therefore intrinsically deviates from unity by at least 1.35%. The second thing to note is the profile of the curve: the correlation declines with the number of multipoles. As previously brought up, the difference in scale factor dependence is a likely cause of this: $C_\ell^{\tau\tau}$ scales as $1/a^4$ whereas C_ℓ^{DMDM} scales as $1/a^2$. This also makes physical sense as differences in the DM signals of FRBs and those arising from the Thomson scattering of the CMB are likely to manifest at smaller scales where departures from isotropy are captured in the finer details of the signals.

5. Signal to Noise Forecasts

In order to assess the merit of correlating the DMs of FRBs with CMB optical depth anisotropies, we need to be able to compare the SNR defined in Eqn. (53) to those of other cross-correlations. The main limiting factor here is the noise term, N_ℓ^{DMDM} given by Eqn. (38). This is because the 2-dimensional FRB number density, n_f^{2d} is poorly constrained. With upcoming surveys using instruments such as the Karoo Array Telescope (MeerKAT) and the Square Kilometre Array (SKA), high rates of FRB detections are anticipated in the near future. Naturally, the first step in assessing the value of a cross-correlation between FRB DMs and CMB optical depth fluctuations would be to keep the number of FRB detections, N_{FRB} as a free parameter and plot the SNR as a function of it. This can be done for several plausible values for the DM variance, σ_{DM}. If the SNR appears to be promising for realistic values of N_{FRB} compared to other cross-correlations, the next step would be to deploy a population synthesis program, `frbpoppy` to impose better priors on the SNR (Gardenier et al. 2019).

5.1. The Noise Term, N_ℓ^{DMDM}

As we can see from Eqn. (14), the noise corresponding to the auto-correlation of the DM is given by

$$N_\ell^{\mathrm{DMDM}} = \frac{\sigma_{\mathrm{DM}}^2}{n_f^{2d}} \tag{37}$$

where n_f^{2d} is the 2-dimensional FRB number density per steradian with a SNR ratio or specific fluence above a specific value, and σ_{DM}^2 is the variance of the DM (Madhavacheril et al. 2021). The denominator here is where the FRBs come in: the higher n_f^{2d} for a given σ_{DM}^2, the lower the noise contribution and vice versa. Because n_f^{2d} the main independent variable in any simulation of the SNR, it will be tackled in Sec. 5.3. That leaves the value for σ_{DM} for discussion here.

5.1.1. The Standard Deviation $\sigma_{\mathrm{DM}}(z)$

Whilst n_f^{2d} mainly depends on intrinsic FRB populations, σ_{DM}, just as the DM itself, depends on the ionisation history along the line of sight. Better measurements on the DMs of a fixed number of FRBs result in smaller values of σ_{DM} and therefore a reduction of the noise. The dependence on the ionisation history means that σ_{DM} varies with redshift. Here, we follow Beniamini et al. (2021) and Jaroszynski (2020) by adopting the approximation

$$\sigma_{\mathrm{DM}} \approx \frac{0.13 \mathrm{DM}_{\mathrm{IGM}}}{\sqrt{1+z}} \tag{38}$$

which is based on an *Illustris* simulation. However, we heed caution with the above relation as it only holds at $0 \leqslant z \leqslant 3$ and is highly uncertain at high redshifts, including the entire EoR.
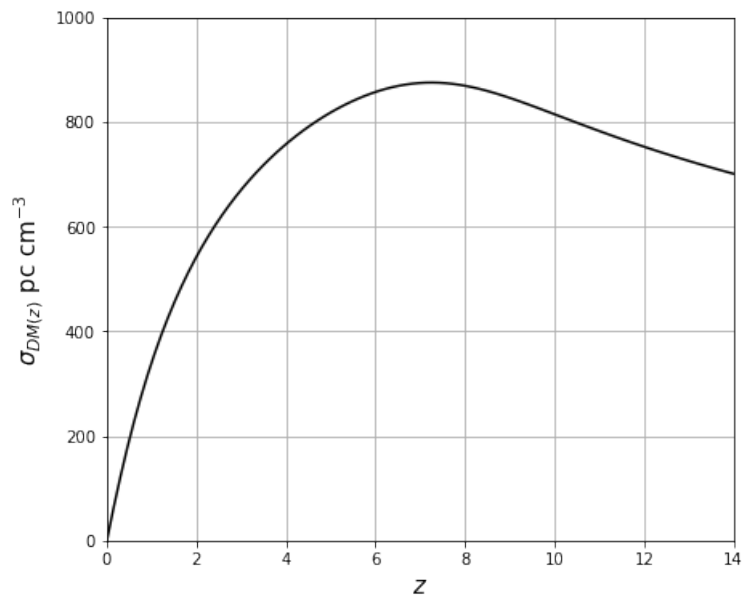

Fig. 10. The standard deviation of the Dispersion Measure as a function of redshift.

As can be seen in Fig. 10, σ_{DM} reaches its maximum value between $z = 6$ and $z = 8$; that is, during the EoR. This no doubt reflects uncertainties in the ionisation history and the time or redshift dependence of the ionisation fraction, x_e. We therefore determine σ_{DM} in the following manner:

1. Define a redshift array using `numpy.linspace(0, 15, 100)`: that is, an array of 100 evenly-spaced values between $z = 0$ and $z = 15$
2. Use Eqns. (10) and (11) to calculate the corresponding DM values
3. Obtain an array of corresponding σ_{DM} values (those plotted in Fig. 10)
4. Calculate the average across the σ_{DM} array using `numpy.mean`: in this case, we find its value to be $711\,\mathrm{pc\,cm^{-3}}$

In light of the dearth of data available to inform a likely profile of N_ℓ^{DMDM} we assume the noise to be flat. Therefore, it serves as a threshold within the context of this thesis to be compared with the corresponding signal of C_ℓ^{DMDM}. In the figure below, we plot the noise values for three different values of the standard deviation in the dispersion measure, σ_{DM} whilst keeping the number of FRBs, N_{FRB} constant, and for three different numbers of FRBs whilst keeping σ_{DM} constant. The signal is also displayed in the plot so to see where it is with respect to the noise.
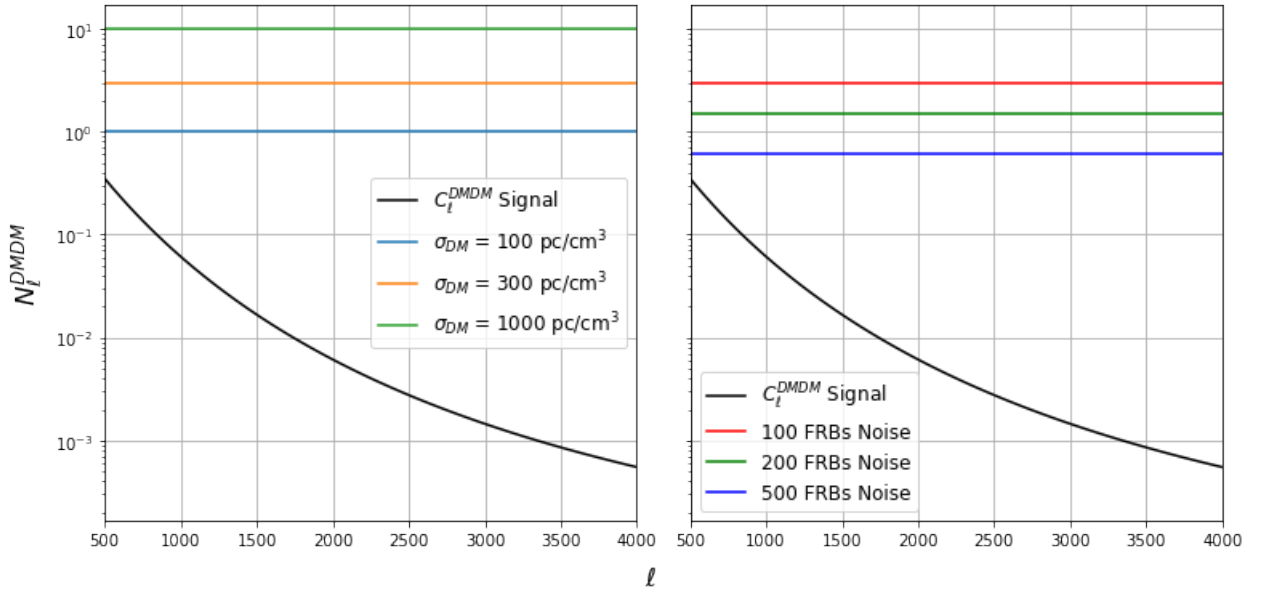

Fig. 11. Left panel: the Dispersion Measure Noise plotted for three different values of σ_{DM} with $N_{\mathrm{FRB}} = 100$. Right panel: the Dispersion Measure Noise plotted for three different quantities of FRBs with $\sigma_{\mathrm{DM}} = 300\,\mathrm{pc\,cm^{-3}}$.

It can be seen from Fig. 13 that in none of the cases is the signal above the noise for the range considered. The case becomes significantly more favourable when the number of FRBs is increased, as opposed to more precise measurements of the DM. The values chosen here for the numbers of FRBs are roughly commensurate with those discovered at the time of writing: 119 FRBs have been confirmed and uploaded to `frbcat.org` (Petroff et al. 2019), and 536 have been reported in the first survey of the CHIME/FRB collaboration (Amiri et al. 2021). It is evident here that N_ℓ^{DMDM} is very sensitive to the number of FRBs. Therefore, even if Dispersion Measure is challenging to constrain and has values on the order of a $\sim 300\,\mathrm{pc\,cm^{-3}}$ or more, the noise can be significantly reduced if enough FRBs are detected. If future surveys detect $\sim 10^3$ FRBs or more (as expected), this threshold should be lowered.

5.2. The Noise Term, $N_\ell^{\tau\tau}$

We have from Meerburg et al. (2013) that the noise on the auto-correlation of the optical depth of CMB anisotropies is given by

$$N_\ell^{\tau\tau} = \left[\frac{1}{2\ell + 1} \sum_{\ell_1 \ell_2} \frac{|\Gamma|_{\ell_1, \ell_2 \ell}^2}{(C_{\ell_1}^{EE} + N_{\ell_1}^{EE})(C_{\ell_2}^{BB} + N_{\ell_2}^{BB})} \right]^{-1} \tag{39}$$

where C_ℓ^{EE} and C_ℓ^{BB} are the E- and B-mode polarisation power spectra respectively, $\gamma_{\ell_1\ell_2\ell}$ is the coupling term, and the two corresponding noise terms are in turn given by

$$N_\ell^{EE} = N_\ell^{BB} = \Delta_P^2 \exp\left(\frac{\ell(\ell+1)\theta_{\mathrm{FWHM}}^2}{8\ln 2}\right) \tag{40}$$

where Δ_P is the detector noise, in this case taken to be $1\,\mu\mathrm{K}$ and θ_{FWHM} is the full-width half maximum of the beam taken to be 1 arcmin. This is known as the reconstruction noise[7] power spectrum as the optical depth anisotropies are not directly measurable but rather are reconstructed using the quadratic estimator, $\hat{\tau}_{\ell m}$. In this case, the values chosen for the detector noise and the full-width half maximum resemble those of the CMB-S4 experiment (Abazajian et al. 2019), just as they do in Namikawa et al. (2021). We refer the reader to Appendix A of Dvorkin & Smith (2009) for a derivation of the above equation. The reconstructed noise profile obtained is shown in the figure below with the corresponding signal superimposed.
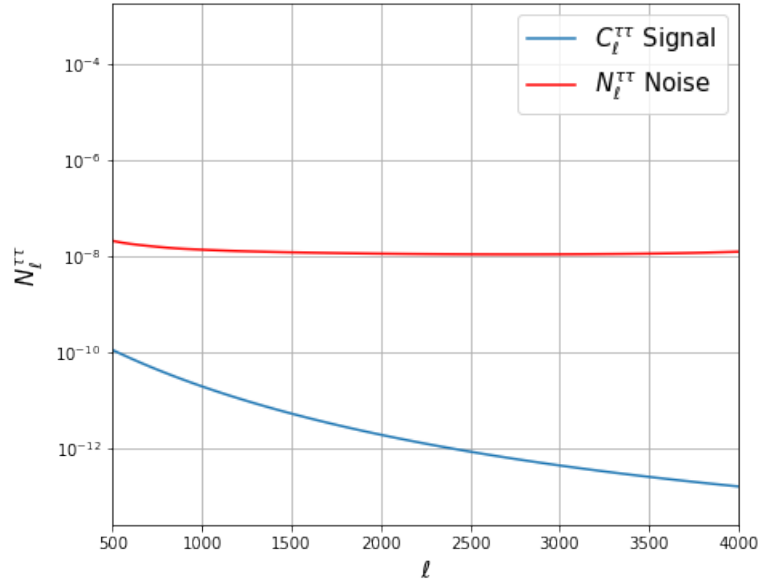

Fig. 12. The Noise Term for τ_{CMB} plotted with the corresponding power spectrum.

In the case of Fig 14, the noise values here are several orders of magnitude higher than those of $C_\ell^{\tau\tau}$. Despite the anisotropies of the optical depth having been constrained by the analyses of Gluscevic et al. (2013); Namikawa (2018) and Feng & Holder (2019), this high reconstruction noise limits most measurements to date (Namikawa et al. 2021). This in part motivates cross-correlating the τ_{CMB}-fluctuations with the DMs of FRBs: if the signal of the cross-spectrum exceeds the corresponding noise by a reasonable amount, the finer details of the IGM during the EoR can be effectively probed in spite of the noise ceiling set by, $N_\ell^{\tau\tau}$. To this end, the Signal-Noise contrast of Fig. 13 is promising. Therefore, we shall derive the SNR of the cross-spectrum in the next subsection and thereby quantify the efficacy of the DMs of FRBs in constraining the EoR.

5.3. Signal to Noise Ratio (SNR)

Now that we have defined relations for both the auto-correlation functions $C_\ell^{\mathrm{DM,DM}}$ and $C_\ell^{\tau\tau}$; their corresponding noise terms, $N_\ell^{\mathrm{DM,DM}}$ and $N_\ell^{\tau\tau}$; and the cross-spectrum, $C_\ell^{\tau\mathrm{DM}}$, we need to determine the Signal-to-Noise Ratio (SNR) associated therewith. Because the variables τ_{CMB} and DM are covariant the noise is dependent on a cross-term of τ_{CMB} and the DM in addition to the terms associated with the auto-correlation functions (including noise). We therefore begin with a derivation of this quantity. The following subsection then details the dependence of the SNR on the number of FRBs discovered together with three different possible values of the standard deviation in the DM as well as three different levels of $N_\ell^{\tau\tau}$. In the final section we simulate a selection of surveys and present an estimate of their SNRs as a function of angular wavenumber, ℓ.

---

[7]Note that this is the full-sky version.

5.3.1. Deriving the SNR

To derive the SNR for a cross-correlation between τ_{CMB} and DM, we need to obtain the corresponding Fisher matrix element given by

$$F_{ij} = \sum_{XY} \sum_{\ell} \frac{\partial C_{\ell}^{XY}}{\partial \theta_i} \left(\beta_{ij}^{XY}\right)^{-1} \frac{\partial C_{\ell}^{XY}}{\partial \theta_j} \tag{41}$$

where β_{ij}^{XY} is ij-th element of the covariance matrix of the variables X and Y whilst θ_i and θ_j are arbitrary parameters upon with the data depends (Verde 2010). In our case, we have $X \in (\tau, \text{DM})$ and $Y \in (\tau, \text{DM})$. We also set $\theta_i = \theta_j = A$ such that

$$\tilde{C}_{\ell}^{\tau\text{DM}} = A C_{\ell}^{\tau\text{DM}} \tag{42}$$

where A is a pivot parameter that determines the amplitude. This is the quantity that we want to measure. By the above definition, we have that

$$\frac{\partial C_{\ell}^{\tau\text{DM}}}{\partial A} = \frac{1}{A} \tag{43}$$

so

$$F_{ij} = \sum_{\ell} \frac{1}{A^2} C_{\ell}^{\tau\text{DM}} \left(\beta_{ij}^{\tau\text{DM}}\right)^{-1} C_{\ell}^{\tau\text{DM}} \tag{44}$$

where the covariance matrix is given by

$$\beta_{\ell}^{\tau\text{DM}} = \frac{2}{2\ell+1} \begin{bmatrix} (C_{\ell}^{\tau\tau})^2 & (C_{\ell}^{\tau\text{DM}})^2 & C_{\ell}^{\tau\tau} C_{\ell}^{\text{DMDM}} \\ (C_{\ell}^{\tau\text{DM}})^2 & (C_{\ell}^{\text{DMDM}})^2 & C_{\ell}^{\text{DMDM}} C_{\ell}^{\tau\text{DM}} \\ C_{\ell}^{\tau\tau} C_{\ell}^{\tau\text{DM}} & C_{\ell}^{\text{DMDM}} C_{\ell}^{\tau\text{DM}} & \frac{1}{2}[(C_{\ell}^{\tau\text{DM}})^2 + C_{\ell}^{\tau\tau} C_{\ell}^{\text{DMDM}}] \end{bmatrix} \tag{45}$$

In this case, we require i and j to correspond to the row and column of τDM, τDM so $i = 3$ and $j = 3$ which we label as AA. Therefore, we may write

$$\beta_{AA}^{\tau\text{DM}} = \frac{1}{2\ell+1} [(C_{\ell}^{\tau\text{DM}})^2 + C_{\ell}^{\tau\tau} C_{\ell}^{\text{DMDM}}] \tag{46}$$

Then, we have

$$F_{\tau\text{DM},\tau\text{DM}} = \frac{1}{A^2} \sum_{\ell} (2\ell+1) \frac{(C_{\ell}^{\tau\text{DM}})^2}{(C_{\ell}^{\tau\text{DM}})^2 + C_{\ell}^{\tau\tau} C_{\ell}^{\text{DMDM}}} \tag{47}$$

We wish to measure A to obtain the SNR as it determines the amplitude of the signal. The noise on A is given by

$$\sigma_A = \frac{1}{\sqrt{F_{AA}}} \tag{48}$$

and since by definition the SNR is A/σ_A, we have

$$\left(\frac{S}{N}\right)^2 = \sum_{\ell} (2\ell+1) \frac{(C_{\ell}^{\tau\text{DM}})^2}{(C_{\ell}^{\tau\text{DM}})^2 + C_{\ell}^{\tau\tau} C_{\ell}^{\text{DMDM}}} \tag{49}$$

As per the formalism of Verde (2010),

$$C_{\ell} \rightarrow C_{\ell} + N_{\ell} \tag{50}$$

and

$$\beta_{AA}^{\tau\text{DM}} \rightarrow \beta_{AA}^{\tau\text{DM}} / f_{\text{sky}} \tag{51}$$

where $f_{\text{sky}} = \Omega/(2\pi)^2$ is the sky fraction of a given survey and Ω is the solid angle over which it is performed. We may also promote the sum to an integral:

$$\sum_{\ell} (2\ell+1) \rightarrow \int \ell d\ell \tag{52}$$

which in combination with all of the steps above results in our final formula for the total SNR:

$$\left(\frac{S}{N}\right)^2 = \frac{\Omega}{(2\pi)^2} \int \ell d\ell \frac{(C_{\ell}^{\tau\text{DM}})^2}{(C_{\ell}^{\tau\tau} + N_{\ell}^{\tau\tau})(C_{\ell}^{\text{DMDM}} + N_{\ell}^{\text{DMDM}}) + (C_{\ell}^{\tau\text{DM}})^2} \tag{53}$$

In this case, there are three variables that can be kept as free parameters, two of which originate from the aforedescribed noise term, $N_{\ell}^{\text{DM,DM}}$. These are the uncertainty in DM itself, σ_{DM} and the number of FRBs detected, N_{FRB}. Although the denominator in Eqn. (37) is technically the number of FRBs per steradian, we have that $n_f^{2d} \approx N_{\text{FRB}}$ provided we assume the distribution of newly discovered FRBs is isotropic. The other free parameter is of course ℓ. As a reminder, this corresponds to an angle on the sky in such a way that larger values correspond to smaller scales and vice versa.

5.3.2. SNR as a function of N_{FRB}

Here, we investigate the dependence of the cross-spectrum's SNR on the number of FRBs detected, N_{FRB}. In order to achieve this, we integrate Eqn. (53) over the entire range of modes considered in this thesis: that is, between $\ell = 0$ and $\ell = 4000$. As previously stated, we use the assumption that $n_f^{2d} \sim N_{\text{FRB}}$ so the number of FRBs is contained within the denominator of the noise term, N_ℓ^{DMDM} defined by Eqn. (37). There are two additional variables we consider here: the uncertainty in the measurement of the DM, manifest in σ_{DM} and the level of reconstruction noise, $N_\ell^{\tau\tau}$ which we simply scale up by an integer value.
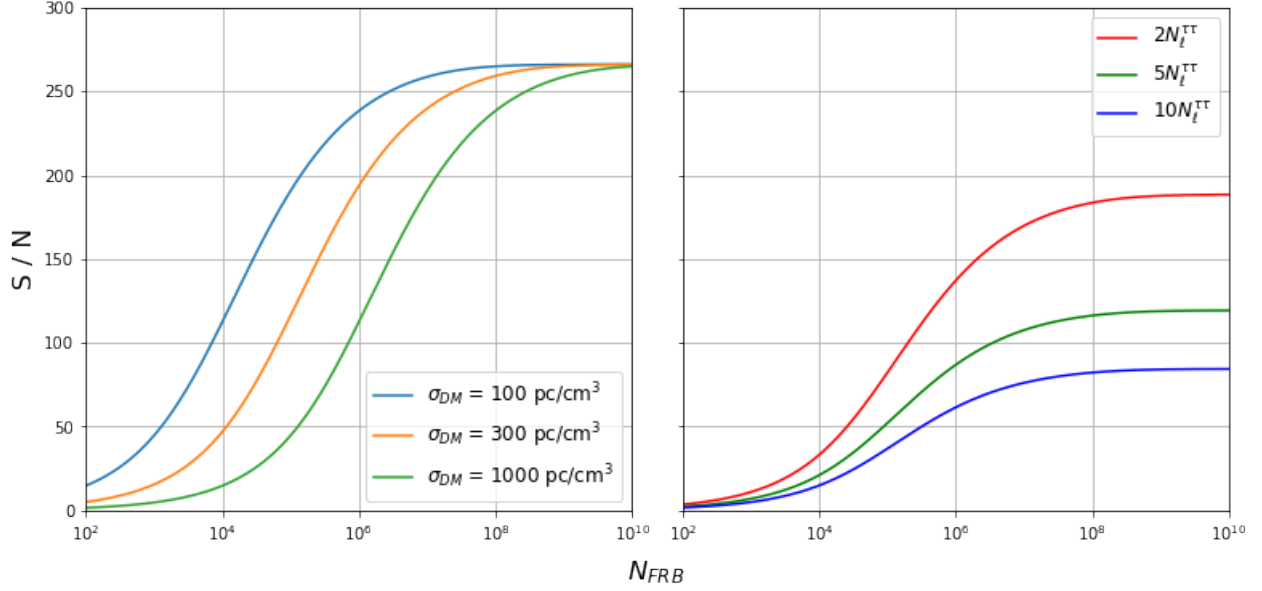

Fig. 13. The Signal to Noise Ratio of the cross-correlation as a function of FRB detections. In the left panel, curves have been plotted for three different standard deviations, σ_{DM} and in the right panel, the surves have been plotted for three different levels of the reconstructed noise of the CMB optical depth fluctuations, $N_\ell^{\tau\tau}$.

The first thing evident from Fig. 13 is the SNR is very sensitive to the number of FRB detections. We also see that the SNR will begin to increase rapidly once the number of FRB detections surpasses $\sim 10^3$. Only at very high values of $N_{\text{FRB}}, \sim 10^8$ does the SNR begin to saturate. As would be expected, fewer FRB detections are needed to reach the rapid growth phase and saturation point for more accurate DM measurements (ie. smaller σ_{DM}). All SNR curves converge at 266 in this particular case.

The right panel of Fig. 13 reveals that the SNR is indeed τ_{CMB}-noise limited. Increasing $N_\ell^{\tau\tau}$ has the effect of lowering the SNR ceiling by an amount directly proportional to the factor preceding $N_\ell^{\tau\tau}$. Therefore, the convergence points too are lowered by a factor of 2, 5 and 10. It should be noted that σ_{DM} is held constant at $300\,\text{pc}\,\text{cm}^{-3}$. The convergence points of the left and right panels are summarised in the table below.

σ_{DM} / $\text{pc}\,\text{cm}^{-3}$	$\times N_\ell^{\tau\tau}$	N_{FRB}	S / N
100	1	6.774×10^8	266
300	1	6.149×10^9	266
1000	1	6.837×10^{10}	266
300	2	1.487×10^9	188
300	5	1.413×10^9	119
300	10	7.887×10^8	84

Now that we have an idea of the dependence of the SNR on N_{FRB}, σ_{DM} and the ceiling set by $N_\ell^{\tau\tau}$, we can perform survey simulations wherein we obtain the SNR profiles as functions of the angular wavenumber (number of multipoles), ℓ. Before proceeding, we note that the SNR values in Fig. 13 have been integrated over the entire range[8] of multipoles considered here; that is, from $\ell = 0$ to $\ell = 4000$. Therefore, the Signal-to-Noise ceiling remains at 266 and the only way to exceed this is to reduce $N_\ell^{\tau\tau}$. In practice, the values of SNR should be much lower than this as at the time

---

[8]The graphs begin at $\ell = 500$ but the integration is performed from $\ell = 0$.

of writing, existing experiments or those under construction are expected to detect at the very most $\sim 10^5$ new FRBs (Madhavacheril et al. 2021).

5.4. Population Synthesis

In order to simulate realistic scale-dependent SNRs for the cross-correlation of FRB DMs and the CMB Anisotropies, we use the population synthesis program, `frbpoppy` (Gardenier et al. 2019). Specifically, it determines the value of n_f^{2d} for a given survey. This then allows the noise term, $N_\ell^{\mathrm{DM\,DM}}$ to be determined which we, for simplicity, assume to be flat with respect to ℓ. Then, we calculate the SNR by integrating up to a maximum angular wavenumber, $\ell_{\max}$. In this subsection, we begin by describing the basics of population synthesis models and then explain differences between each of the surveys we simulate: these are embodied in a single plot of the SNR against $\ell_{\max}$, which will be followed by a brief analysis of the results to conclude this section.

5.4.1. The Basics

There are two main steps involved in simulating an FRB survey:

1. Generating an intrinsic population of FRBs
2. Determining the fraction above a SNR or fluence threshold

In this regard, the first point is informed by an inference of the number of FRBs emitted over a comoving volume. This is in addition to the free electron density along the line of sight. Since we know the technical limitations of instrumentation that we could use, the second step is applied somewhat more easily.

5.4.2. Generating an FRB Population

It is relatively easy to overlook that the sources of FRBs are still rather elusive. Whilst this may not be a priority to those seeking to use them as cosmological probes, it could precipitate errors when trying to infer their redshift distribution. The redshift dependence of FRB number density depends heavily on the nature of the phenomenon itself. The current consensus is that FRBs are caused by magnetars (Petroff et al. 2019); that is, neutron stars with extremely high magnetic fields (Cline et al. 1982; Kaspi & Beloborodov 2017; Beniamini et al. 2021). This would imply at the very least that the volumetric rate of FRBs is coupled to the underlying Stellar Mass Density and as a consequence, the Initial Mass Function (IMF) and Star Formation Rate (SFR). Beniamini et al. (2021) go a step further and compare it with the magnetar formation rate, using the IMF of Kroupa (2001). However, the model employed by Gardenier et al. (2019) is much simpler and based on the following proportionality relation:

$$n_{\mathrm{FRB}}(z) \propto \int_0^\infty \frac{(1+z')^{2.7}}{1+[(1+z')/2.9]^{5.6}} \frac{dz'}{H(z')} \tag{54}$$

where n_{FRB} is the number density of FRBs and $H(z')$ is the Hubble parameter assuming a flat Universe ($\Omega_\kappa = 0$) (Madau & Dickinson 2014; Gardenier et al. 2019). Furthermore, the comoving volume of an FRB is given by

$$V_{\mathrm{co,\,FRB}} = V_{\mathrm{co,\,max}} U(0,1)^\beta \tag{55}$$

where $V_{\mathrm{co,\,max}}$ is the maximum value it can assume, $U(0,1)$ is a random number from a uniform distribution with $U \in [0,1]$. β is an exponent that corresponds to a bias in the redshift distribution of the FRB sources and follows a power law:

$$\beta = -\frac{3}{2\alpha_{\mathrm{in}}} \tag{56}$$

where α_{in} is an input parameter that can be adjusted based on a chosen model (see Fig. 1 in Gardenier et al. (2019)). This completes a basic description of how an FRB population is generated in `frbpoppy`.

5.4.3. Simulating a Survey

Now to simulate a survey, we need to establish the fraction of an intrinsic population that would be observable to us. This would depend on the survey and the constraints of the instrumentation therein. Rather than repeating all of the finer

details that can be found in Gardenier et al. (2019), we restrict our discussion here to the receiver[9] SNR and the beam pattern at the receiver: the former because it embodies the detection threshold and the latter because it is a variable that can be changed as an input.

In this context, the detection threshold is set by a minimum SNR. This is determined from the following equation:

$$\text{S/N} = \frac{\bar{S}_\text{peak} G}{\beta_\text{deg} T_\text{sys}} \sqrt{n_\text{pol}(\nu_2 - \nu_1) w_\text{aff}} \tag{57}$$

where $\bar{S}_\text{peak}$ is the peak flux density, G is the gain, β_deg is the degradation factor, T_sys is the total system temperature, n_pol is the number of polarisations, $\nu_{1,2}$ are the boundary frequencies of a given survey and w_aff is the pulse width at Earth (Lorimer & Kramer 2012; Connor 2019; Gardenier et al. 2019). More detailed explanations of each of these variables, including the log-normal distribution of pulses are given in Gardenier et al. (2019). This equation is the radiatometer equation for a single pulse. T_sys, w_arr and $\bar{S}_\text{peak}$ are the variables that depend on the FRBs themselves and the rest are those that depend on the survey and the instrumentation used therefor.

As for the beam pattern, there are several options available. In this thesis, the Parkes and Apertif beam patterns are chosen to match their corresponding simulated surveys (Ravi et al. 2016; Adams & van Leeuwen 2019). The perfect simulated survey assumes a perfect intensity profile:

$$I(r) = 1 \tag{58}$$

where r is the scaled angular distance on the sky from the beam centre $r \in [0, 1]$. For all other simulated surveys, the beam pattern is assumed to be Gaussian:

$$I(r) = e^{-r^2 M^2 \ln 2} \tag{59}$$

where M is a scaling factor defined in Appendix A of Gardenier et al. (2019) and r has the same meaning as in Eqn. (59). This profile was chosen for simplicity and consistency between the other simulated surveys.

5.4.4. Results

Using the population synthesis program `frbpoppy`, we generate values of n_f^{2d} corresponding to the number of FRBs detected in a given survey. Simultaneously, an average value of σ_DM is calculated using Eqn. (38). Armed with values for σ_DM and n_f^{2d}, the noise term $N_\ell^{\text{DM DM}}$ is calculated using Eqn. (37) for each of the surveys. This in turn is used as an input in Eqn. (39) where the integration up to a maximum multipole, ℓ_max is approximated by multiplying the integrand evaluated at ℓ_max by the corresponding $d\ell$ (found using `numpy.diff()`) and then taking a cumulative discrete sum over all the products using `itertools.accumulate()`. Ω for each of the surveys is determined from the corresponding field-of-view in Gardenier et al. (2019). The following plot was obtained for all of the survey simulations available on `frbpoppy` using the aforedescribed method and the aforementioned choices of input:

---

[9]Not to be confused with the SNR of the cross-correlation referred to throughout this thesis.
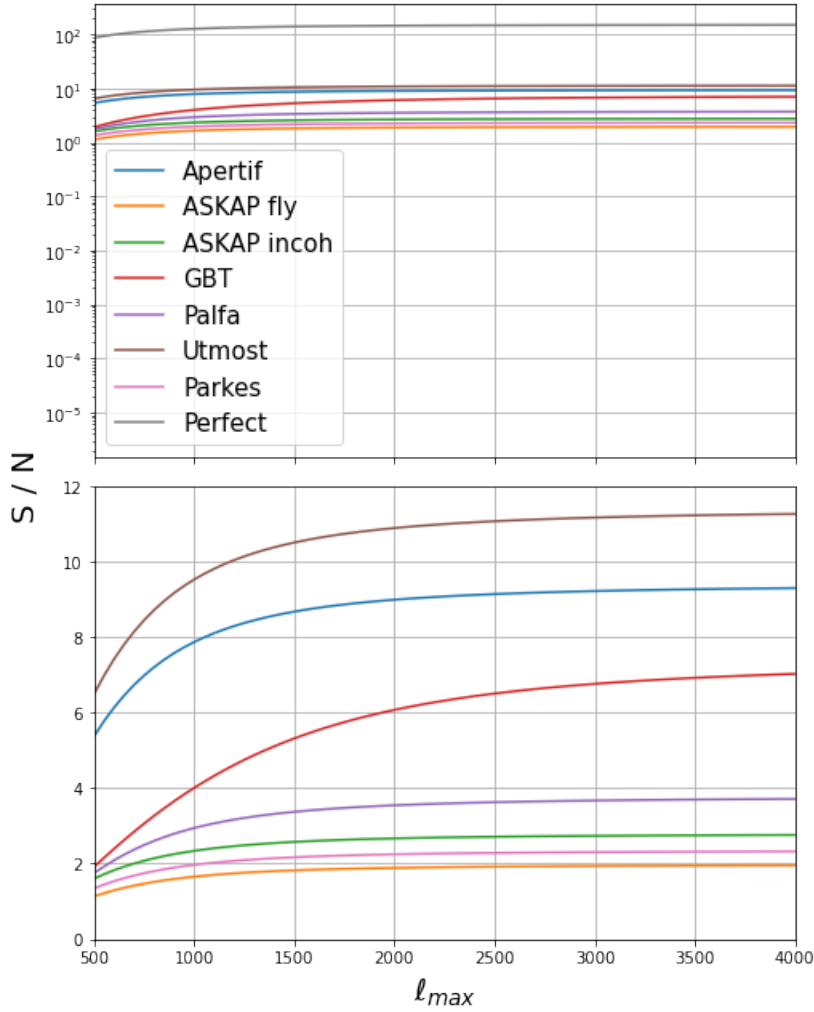
Fig. 14. Top panel: SNR as a function of ℓ_{max} plotted with a logarithmic y-axis so that the perfect survey can be seen in the same plot as the others. Bottom panel: the SNR as a function of ℓ_{max} plotted with a linear y-axis and a range suitable for all curves except from that of the perfect survey to be visible.

In Fig. 14, we see, as expected that the "Perfect" survey has the highest overall values for the SNR. That said, its SN curve converges at 150 which is a little over half the 266 SN-ceiling set by $N_\ell^{\tau\tau}$. This very likely to be a result of the detection threshold defined by Eqn. (57). In other words, there is an intrinsic limit to the number of FRBs that can be detected in the surveys that can be simulated by `frbpoppy`. As the threshold is set by a minimum (raw) SNR at the hypothetical detector, this is likely to be a consequence of the minimum possible degradation factor, β_{deg} and the maximum possible value of the gain, G available on the program. Naturally, all the "real" simulated surveys exhibit SNR values significantly lower than this. Most seem to have SNRs on the order of ~ 10 or less, with the SNR increasing rapidly up to a maximum number of multipoles, ℓ_{max} of 1000. By $\ell_{\mathrm{max}} = 2000$ most of the curves have at the very least begun to saturate. In the following table, we list the values of the SNR at which each survey converges.

Survey	n_f^{2d}	S / N
Apertif	8678	9
ASKAP fly	20	1
ASKAP incoh	328	2
GBT	59295689	7
Palfa	1044529	3
Utmost	14309	11
Parkes	8403	2
Perfect	473	150

6. Discussion

We investigated the correlation between two quantities: the DM of FRBs and τ_{CMB} anisotropies, both of which trace the distribution of free electrons in the IGM and in turn the evolving ionisation fraction during the EoR. In our specific case, we proposed measuring the DM of FRBs as they should be detectable at the redshift interval we are concerned with: that is, principally between $z = 5$ and $z = 10$. FRBs could therefore be used as a backlight for probing the intervening medium and the EoR. To date, the CMB τ_{CMB} anisotropies have been a favoured tool to this end. However, the high levels of reconstructed noise hamper this method's efficacy as a probe. As we have seen in this thesis, the SNRs arising from the correlation between τ_{CMB} and DM yield substantial SNRs with values as high 266 given a sufficient number of detections. In this section, we shall begin by summarising the achievements brought about by the theoretical exercise conducted in this thesis and their wider implications. We then discuss the limitations of the models and strategies used. Then, finally, we explore future prospects in using this method to probe the EoR and conclude with some ideas on the physical uses of this cross-correlation.

6.1. Achievements

There are three main achievements of note in this thesis. The first is evident in Sec. 4.3 where we have established there is at least a 98% correlation between DM and τ_{CMB} at scales between $\ell = 500$ and $\ell = 4000$, as was expected given that both are tracers of the free electron distribution. The second achievement is the finding of Sec. 5.3.2 where we have found that the SNR is τ_{CMB}-limited and despite this, can reach values as high as 266 for the $N_\ell^{\tau\tau}$ noise levels present in the CMB S4 experiment. Thirdly, the simulations performed using the population synthesis program `frbpoppy` by Gardenier et al. (2019) revealed that we expect most contemporary surveys to yield SN-values of 10 or less.

6.1.1. Cross-Correlation Coefficient

We found that the cross-correlation coefficient, $|\alpha|^{\tau\mathrm{DM}}$ is in excess of 98% for the multipole range considered in this thesis: $\ell = 500$ to $\ell = 4000$. However, it does not remain constant as the number of multipoles increases. Rather, that it undergoes a steady decline up until $\ell = 2500$ from which it levels off to a minimum at $\ell = 4000$.

As previously explained, the excess of 98% correlation is a natural consequence of the fact that both τ_{CMB} and DM are tracers of the free electron distribution. In the context of the reionisation model used here (Wang & Hu 2006; Namikawa et al. 2021), there are only two distinguishing features: the Thomson scattering cross-section contribution, σ_T from τ_{CMB} and the extra $1/a$ dependence from τ_{CMB}.

Given that σ_T is of the order $\sim$ the difference in prefactors cannot be the cause of the disparity. This leaves the additional $1/a$ contribution from τ_{CMB} as the only possible explanation. The fact that the correlation declines - albeit minimally - with increasing ℓ corroborates this. As would be expected, the faster dilution of the Thomson scattered CMB with respect to the dispersed FRBs results a reduction in the correlation of finer details.

The apparent minimum at $\ell \sim 4000$ is more difficult to explain as there is no immediately obvious reason for the correlation to begin increasing again from that point onward. This could be a numerical artefact carried forward from $P_{x_e x_e}$. In this case it cannot be asserted that the Limber approximation is to blame as the findings of Simon (2007) imply, for the Limber approximation generally holds better at large ℓ (Fang et al. 2020). Another possibility is that at smaller scales, the correlation increases owing to overdensities of free electrons in regions associated with matter. Namely, if we assume that the majority of high-energy photons given off during the EoR originated in galaxies, the surrounding IGM would have been ionised first. Since τ_{CMB} is a tracer of the free electron number density by virtue of the aforementioned kinematic Sunyaev Zeldovich (kSZ) effect and DM is a tracer of the free electron number density via the dispersion of FRB signals[10], the correlation could marginally increase at smaller scales.

6.1.2. Signal-to-Noise Ceiling

The first main finding from Fig. 13 is that the SNR increases rapidly from approximately 10^3 and does not saturate until $\sim 10^8$. This sensitivity to the number of FRB detections and the relatively low level of noise with respect to τ_{CMB} alone renders this cross-correlation a promising tool for probing the EoR. The second main finding is that the SNR appears to only be limited by the τ_{CMB}-noise and even with $N_{\mathrm{FRB}} \sim 10^2$ has values on the order of ~ 10 for $\sigma_{\mathrm{DM}} = 300\,\mathrm{pc\,cm}^{-3}$. This is confirmed by the plot on the right panel of Fig. 13 which shows that scaling up the noise from an CMB S4-like

---

[10]Presumably originating in galaxies.

experiment suppresses the SNR by values directly proportional to the factor preceding $N_\ell^{\tau\tau}$ (Abazajian et al. 2019). In spite of this, the SNR can reach values greater than 50; even if noise levels are $10\times$ higher than that of the CMB S4 experiment.

6.1.3. Simulated Surveys

The final results of note were provided by the population synthesis program `frbpoppy` (Gardenier et al. 2019). Here, the program generated FRBs, a fraction of which had a sufficiently strong signal to exceed the Signal-to-Noise threshold of a given detector defined by Eqn. (57). The SNR was obtained by integrating across the entire redshift range from $z = 5$ to $z = 15$. The results in Fig. 14 are plotted cumulatively, as a function of the maximum angular wavenumber, $\ell_{\max}$.

Whilst the number of detections sets a theoretical SNR ceiling limited by $N_\ell^{\tau\tau}$, the "perfect" survey lowers this by introducing an additional intrinsic detection threshold which in this case corresponds to a SNR of 150. The simulated surveys modify the detector variables in Eqn. (6) in accordance with those of the surveys listed. Among these, the UTMOST survey, of which the technical details are described in Bailes et al. (2017) attained the highest values, saturating at a SNR of 11 . This was closely followed by Apertif which at similar values of $\ell_{\max}$ levelled off at a SNR of 9 (Maan & van Leeuwen 2017). In most cases, the SNR remains relatively unchanged for $\ell_{\max} > 2000$. The surveys that converge at lower SNR values also tend to saturate earlier.

6.2. Limitations

The fundamental limitation in using the cross-correlation between the DMs of FRBs and τ_{CMB} anisotropies is the current dearth of data on FRBs. Whilst there is an emerging consensus that FRBs are produced by magnetars[11] (Bochenek et al. 2020; CHIME/FRB Collaboration et al. 2020; Madhavacheril et al. 2021), this assumption is by no means conclusive. This is important in the context of this cross-correlation because it means that not only is the number density of FRBs dependent on the redshift, but it also dependent on the star formation rate and the fraction of stars massive enough and with a strong enough magnetic field to give rise to a magnetar. In the population synthesis models of Gardenier et al. (2019), this affects the FRB number density via the proportionality relation of Eqn. (54) which in turn originates from Madau & Dickinson (2014). This is very approximate as it does not fully account for the fraction of stars that result in magnetars. Beniamini et al. (2021) devise a more sophisticated model that tackles this problem by devising a magnetar formation rate as well, building upon the work of Miller & Scalo (1979) and Chabrier (2003) who worked on the neutron star formation rate.

Furthermore, we saw that the signal-to-noise ceiling is set by $N_\ell^{\tau\tau}$. Therefore, the reconstruction noise that limits measurements in Namikawa et al. (2021) by extension limits the measurements that can be made by cross-correlating τ_{CMB} with FRB DMs. This quantity is mainly contaminated by gravitational lensing of the CMB which in turn generates non-Gaussian signals. Although Namikawa et al. (2021) have used "bias-hardened" estimators to mitigate this effect, the additional mode couplings induced by lensing and point sources would still be limiting factors in future surveys.

6.3. Future Prospects

Naturally, there are two paths to improve this cross-correlation: reducing the noise on τ_{CMB} measurements and detecting more FRBs whilst measuring their DMs with greater precision. Therefore, we start this subsection by exploring what can be done to improve the former; that is, to increase the signal-to-noise ceiling by reducing the noise term $N_\ell^{\tau\tau}$ or at least increasing C_ℓ^{DMDM} or $C_\ell^{\tau\mathrm{DM}}$. Then, we conclude this thesis with a discussion on reducing σ_{DM}, detecting more FRBs and extracting more cosmological information from them.

6.3.1. Improving the τ_{CMB} Map

As mentioned in Sec. 6.2, the greatest shortcomings of the τ_{CMB} anisotropy map lie in the extent of lensing and point-source bias mitigation. By this we refer to some of the additional mode couplings in the CMB that may be induced via gravitational lensing or emission by point sources such as stars and galaxies. With future surveys, the use of a *quadratic* estimator used by Namikawa et al. (2021) would be insufficient for their expected sensitivities. Guzman & Meyers (2021) propose using a neural network, ResUNet-CMB to reconstruct anisotropies generated by lensing simultaneously with

---

[11] Highly magnetised neutron stars.

those generated by patchy reionisation. Guzman & Meyers (2021) find that this significantly outperforms quadratic estimators at low noise levels. It should also be noted however that the noise levels where they find significant gains to seem possible are much lower than those of currently planned CMB surveys. This brings us to the main point of improvement for the τ_{CMB} side of matters: a reduction in the reconstruction noise. As we can see from Eqns. (39) and (40), this depends on the detector noise, Δ_P and the angle subtended by the FWHM, θ_{FWHM}. These values need to be reduced in order to lower $N_\ell^{\tau\tau}$ and as a consequence, the aforementioned signal-to-noise ceiling.

6.3.2. FRB Detections

There are two ways in which the $\tau-\mathrm{DM}$ SNR can be maximised by detecting FRBs: the first is by improving measurements of the DM and reducing σ_{DM}; the second is simply by detecting more FRBs, as shown by Fig. 13. Like the signal-to-noise ceiling imposed by $N_\ell^{\tau\tau}$, both of these improvements are a technical matter. However, actually being able to detect sufficient numbers of FRBs and localise them to a redshift is more challenging. This is vital as it is what allows us to extract information on the EoR.

Recall that we assumed $\sigma_{\mathrm{DM}} = 711\,\mathrm{pc\,cm}^{-3}$, the average value for the redshift range considered. As mentioned before, Fig. 10 shows that σ_{DM} is variable and peaks at $z \sim 7$, during the EoR. As a theoretical exercise, this thesis has therefore considered the overall SNR. In practice, however, we recommend ensembles of FRBs to be binned by DM and z before performing the cross-correlation, as suggested by Beniamini et al. (2021). This would be necessary to extract important quantities such as the x_e in a given z-slice.

The greatest source of uncertainty in measuring the DM of a given FRB would be determining the host galaxy's contribution to it. If we write,

$$\sigma_{\mathrm{DM}} = \sigma_{\mathrm{DM}_{\mathrm{MW}}} + \sigma_{\mathrm{DM}_{\mathrm{H}}} + \sigma_{\mathrm{DM}_{\mathrm{IGM}}} \tag{60}$$

where each term gives the uncertainty corresponding to those in Eqn. (12), $\sigma_{\mathrm{DM}_{\mathrm{H}}}$ would inevitably dominate. To minimise this, we need to firstly associate as many FRBs with their host galaxies as possible and secondly, to understand the z-dependence of the host galaxies' physical environments. This would require inferences to be made on the FRB rate and integrated Ultraviolet Luminosity Function (UVLF) in a given galaxy. Whilst the z-dependence of latter quantity can be inferred by investigations into the cosmic star-formation history such as that by Madau & Dickinson (2014), the former is considerably more difficult as there is still no consensus on what physical processes are responsible for FRBs. Beniamini et al. (2021) presume with good reason that magnetars are responsible and define a magnetar formation rate that depends on the Star Formation Rate (SFR), the fraction of stars that bequeath neutron stars and the fraction of neutron stars with a strong enough magnetic field to become a magnetar. Whilst sources such as Bochenek et al. (2020) and CHIME/FRB Collaboration et al. (2020) give credence to the magnetar hypothesis, a firm consensus on FRB origins remains to established. Alternative hypotheses include AGN afterglows (Vedantham et al. 2016), superconducting cosmic strings (Yu et al. 2014; Thompson 2017a,b), exploding black holes Barrau et al. (2014) and many more (Cordes & Chatterjee 2019).

Though the processes responsible for FRBs may seem to be of secondary importance to their utility as a cosmological probe, they are by no means irrelevant: to reduce $\sigma_{\mathrm{DM}_{\mathrm{H}}}$ and consequently σ_{DM}, we need to account for processes in the FRB's immediate environment that may alter its DM; to correctly determine n_f^{2d} in Eqn. (37) for a given z-slice or DM bin, we need to to have priors on the FRB rate and spatial distribution[12]. Therefore, it is important to understand the processes underlying FRBs for them to be used successfully as cosmological probes.

6.4. Physical Implications

Given that the SNR values are all in excess of unity, the $\tau_{\mathrm{CMB}} - \mathrm{DM}$ cross-correlation should indeed be a valuable tool for probing the EoR. In this final subsection of the discussion, we infer some of the potential uses of its signal in order to inspire future work. In particular, it can be weaponised to shatter the degeneracy between primordial contributions to the τ_{CMB} anisotropies and secondary contributions from free electrons during the EoR. This means that not only can we better constrain the onset and duration of the EoR, and the $x_e(z)$ profile therein; it also means we can better constrain fundamental cosmological parameters embodied in the τ_{CMB}-map. Thus, we delineate this subsection into two components: the first where we deal with the information that can be gathered on the EoR and the second where we deal with that that we can attain on fundamental cosmological parameters as a consequence.

---

[12]For example: do we expect there to be just one or several detectable FRBs associated with single host galaxies? How would their number density vary as a function of z? Can we construct an n_{FRB}-map in an analogous way to that of τ_{CMB}?

6.4.1. Epoch of Reionisation

There are three lines of attack in using the DMs of FRBs to probe the EoR on their own, as found in Beniamini et al. (2021): (i) determining the maximum dispersion measure, DM_{max} of FRBs detected in a given survey to constrain the onset of the EoR; (ii) binning the DMs of FRBs in terms of z to gain more insight into their frequency through the EoR and (iii) measuring the redshift of a small sample of $z > 6$ FRBs to within $5 - 10\%$ accuracy in order to better constrain $x_e(z)$ through the EoR.

Meanwhile, the construction of a new τ_{CMB}-map using data from the CMB-S4 survey should yield better constraints on EoR contributions to the CMB temperature and polarisation (Abazajian et al. 2019). Since the formalism for the τ_{CMB}-DM cross-correlation should allow the two quantities to be associated on a statistical basis, localising the FRBs may enable information to be extracted on contributions to CMB temperature and polarisation at a given redshift. In other words, this would directly provide a framework to test our models of the EoR: principally its onset, duration and the redshift profile of the average ionisation fraction. The extent of the correlation embodied by the quantity $|\alpha|^{\tau^{DM}}$ could then be used as a metric to gauge the coherence of a given model of the reionisation history. Whilst further details on how exactly this may be achieved lie beyond the scope of this thesis, the framework established herein should open an avenue for further work on this matter.

6.4.2. Fundamental Cosmological Parameters

Principally, we can obtain constraints on fundamental cosmological parameters by disentangling primordial contributions to the τ_{CMB} anisotropies from those augmented during the EoR and by other physical processes such as gravitational lensing. Whilst FRB signals should in theory be observable *ad initium*[13], secondary contributions to the τ_{CMB}-map should cease beyond the redshift corresponding to the onset of the EoR. This means that if a sufficient number of FRBs can be localised to redshifts beyond the onset of reionisation, the secondary contributions to τ_{CMB} should drop out from the τ_{CMB}-DM SNR and as a consequence, leave behind the primordial τ_{CMB} contribution.

In terms of the specific parameters that can be measured, it is logical to start with the cosmological growth rate. Here we may make use of the kinematic Sunyaev-Zeldovich (kSZ) effect: one of the contributions to the τ_{CMB}-map whereby the CMB photons Compton scatter off free electrons in the IGM and subsequently become Doppler shifted with their bulk radial velocities. As stipulated in Madhavacheril et al. (2021), at large scales linear theory holds and the velocity reconstruction from kSZ tomography is directly proportional to the cosmological growth rate. Therefore, additionally accounting for the kSZ effect in the high-ℓ regime, the cross-correlation between τ_{CMB} and DM can be used to analogously probe the cosmological growth rate before and after the EoR. This in turn can be affected by massive neutrinos, dark energy perturbations and modifications to General Relativity. Thus, obtaining constraints on the growth rate could indirectly serve as a test of predictions from those theories.

---

[13]FRBs should at least be visible from when the Universe's first generation of stars died, $z \leqslant 20$.

7. Conclusion

In this thesis, we set out to examine whether the DMs of FRBs can be used in a cross-correlation with the map of τ_{CMB} anisotropies to probe the EoR. Firstly, we found the two variables to have a correlation exceeding 98% for scales between $\ell = 500$ and 4000. After augmenting the respective auto-correlation noise terms $N_\ell^{\tau\tau}$ and N_ℓ^{DMDM}, we found SNR values well in excess of unity. We firstly demonstrated via Eqn. (37) the noise dependence on the number of FRB detections and the standard deviation in DM measurements. We see that the SNR saturates at 266 regardless of σ_{DM}; what varies is the number of FRBs at which this value is reached, varying from $\sim 10^8$ for $\sigma_{\mathrm{DM}} = 100\,\mathrm{pc\,cm^{-3}}$ to 10^{10} for $\sigma_{\mathrm{DM}} = 1000\,\mathrm{pc\,cm^{-3}}$. The limiting factor here is $N_\ell^{\tau\tau}$, which sets a ceiling for the SNR, as evidenced by the saturation point being lowered from 266 through 188 and 119 to 84 as $N_\ell^{\tau\tau}$ is respectively multiplied by 2, 5 and 10. The surveys simulated using `frbpoppy` generally returned SNR values of ~ 10 and below, but all clearly above unity. To date, Amiri et al. (2021) report 536 FRB detections in a survey done over the course of a year. With expected discovery rates for instruments like HIRAX[14] being on the order of 10 sub-arcsecond localisable FRBs per day (Berger et al. 2016), it is evident that the SNRs presented here are unlikely to reach their saturation points any time soon. Thus cross-correlating FRB DMs with τ_{CMB} anisotropies has significant potential for probing the EoR.

---

[14]Hydrogen Intensity and Real-time Analysis eXperiment

8. Acknowledgements

References

Abazajian, K., Addison, G., Adshead, P., et al. 2019, arXiv preprint arXiv:1907.04473
Adams, E. A. & van Leeuwen, J. 2019, Nature Astronomy, 3, 188
Amiri, M., Andersen, B. C., Bandura, K., et al. 2021, arXiv preprint arXiv:2106.04352
Amiri, M., Bandura, K., Berger, P., et al. 2018, The Astrophysical Journal, 863, 48
Bailes, M., Jameson, A., Flynn, C., et al. 2017, Publications of the Astronomical Society of Australia, 34
Barrau, A., Rovelli, C., & Vidotto, F. 2014, Physical Review D, 90, 127503
Beniamini, P., Kumar, P., Ma, X., & Quataert, E. 2021, MNRAS, 502, 5134
Berger, P., Newburgh, L. B., Amiri, M., et al. 2016, in Ground-based and Airborne Telescopes VI, Vol. 9906, International Society for Optics and Photonics, 99060D
Bochenek, C. D., Ravi, V., Belov, K. V., et al. 2020, Nature, 587, 59
Chabrier, G. 2003, PASP, 115, 763
Chen, S.-y., Maksimchuk, A., & Umstadter, D. 1998, Nature, 396, 653–655
CHIME/FRB Collaboration, Andersen, B. C., Bandura, K., et al. 2019, ApJ, 885, L24
CHIME/FRB Collaboration, Andersen, B. C., Bandura, K. M., et al. 2020, Nature, 587, 54
Cline, T. L., Desai, U. D., Teegarden, B. J., et al. 1982, The Astrophysical Journal, 255, L45
Connor, L. 2019, Monthly Notices of the Royal Astronomical Society, 487, 5753
Cordes, J. M. & Chatterjee, S. 2019, Annual Review of Astronomy and Astrophysics, 57, 417
Dvorkin, C., Hu, W., & Smith, K. M. 2009, Physical Review D, 79, 107302
Dvorkin, C. & Smith, K. M. 2009, Physical Review D, 79
Eftekhari, T. & Berger, E. 2017, ApJ, 849, 162
Fang, X., Krause, E., Eifler, T., & MacCrann, N. 2020, Journal of Cosmology and Astroparticle Physics, 2020, 010
Feng, C. & Holder, G. 2019, Physical Review D, 99
Furlanetto, S. R., Zaldarriaga, M., & Hernquist, L. 2004, The Astrophysical Journal, 613, 1
Gardenier, D., van Leeuwen, J., Connor, L., & Petroff, E. 2019, Astronomy & Astrophysics, 632, A125
Gluscevic, V., Kamionkowski, M., & Hanson, D. 2013, Physical Review D, 87
Gunn, J. E. & Peterson, B. A. 1965, ApJ, 142, 1633
Guzman, E. & Meyers, J. 2021, arXiv preprint arXiv:2101.01214
Ioka, K. 2004, Frontier in Astroparticle Physics and Cosmology, 403
Jaroszynski, M. 2020, arXiv preprint arXiv:2008.04634
Kaspi, V. M. & Beloborodov, A. M. 2017, Annual Review of Astronomy and Astrophysics, 55, 261
Kroupa, P. 2001, Monthly Notices of the Royal Astronomical Society, 322, 231
Kulkarni, G., Keating, L. C., Haehnelt, M. G., et al. 2019, Monthly Notices of the Royal Astronomical Society: Letters, 485, L24
Lewis, A., Challinor, A., & Lasenby, A. 2000, The Astrophysical Journal, 538, 473
Lorimer, D. R. & Kramer, M. 2012, Handbook of Pulsar Astronomy
Maan, Y. & van Leeuwen, J. 2017, in 2017 XXXIInd general assembly and scientific symposium of the international union of radio science (URSI GASS), IEEE, 1–4
Madau, P. & Dickinson, M. 2014, Annual Review of Astronomy and Astrophysics, 52, 415
Madhavacheril, M., Battaglia, N., Smith, K., & Sievers, J. 2021, arXiv preprint arXiv:1901.02418
Masui, K. W., Shaw, J. R., Ng, C., et al. 2019, Algorithms for FFT Beamforming Radio Interferometers
McGreer, I. D., Mesinger, A., & D'Odorico, V. 2014, Monthly Notices of the Royal Astronomical Society, 447, 499–505
Meerburg, P. D., Dvorkin, C., & Spergel, D. N. 2013, The Astrophysical Journal, 779, 124
Miller, G. E. & Scalo, J. M. 1979, ApJS, 41, 513
Namikawa, T. 2018, Physical Review D, 97
Namikawa, T., Roy, A., Sherwin, B. D., Battaglia, N., & Spergel, D. N. 2021, Phys. Rev. D, 104, 063514
Nordgren, T. E., Cordes, J., & Terzian, Y. 1992, The Astronomical Journal, 104, 1465
Oesch, P. A., Brammer, G., van Dokkum, P. G., et al. 2016, ApJ, 819, 129
Pagano, M. & Fronenberg, H. 2021, Monthly Notices of the Royal Astronomical Society, 505, 2195
Petroff, E., Hessels, J., & Lorimer, D. 2019, The Astronomy and Astrophysics Review, 27, 1
Rafiei-Ravandi, M., Smith, K. M., & Masui, K. W. 2020, Phys. Rev. D, 102, 023528
Ravi, V., Shannon, R., Bailes, M., et al. 2016, Science, 354, 1249
Simon, P. 2007, Astronomy & Astrophysics, 473, 711
Sokasian, A., Abel, T., & Hernquist, L. 2002, Monthly Notices of the Royal Astronomical Society, 332, 601–616
Sun, G. & Furlanetto, S. R. 2016, Monthly Notices of the Royal Astronomical Society, 460, 417
Sunyaev, R. A. & Zeldovich, Y. B. 1980, MNRAS, 190, 413
Taylor, J. H. & Cordes, J. 1993, The Astrophysical Journal, 411, 674
Thompson, C. 2017a, The Astrophysical Journal, 844, 65
Thompson, C. 2017b, The Astrophysical Journal, 844, 162
Vedantham, H., Ravi, V., Mooley, K., et al. 2016, The Astrophysical Journal Letters, 824, L9
Verde, L. 2010, in Lectures on Cosmology (Springer), 21
Wang, X. & Hu, W. 2006, The Astrophysical Journal, 643, 585
Wyithe, J. S. B. & Loeb, A. 2003, The Astrophysical Journal, 586, 693
Yu, Y.-W., Cheng, K.-S., Shiu, G., & Tye, H. 2014, Journal of Cosmology and Astroparticle Physics, 2014, 040
Zhang, B. 2018, ApJ, 867, L21